

# RAG-GNN: Integrating Retrieved Knowledge with Graph Neural Networks for Precision Medicine

Hasi Hays<sup>1,\*</sup> and William J. Richardson<sup>1</sup>

<sup>1</sup>Department of Chemical Engineering, University of Arkansas, Fayetteville, AR 72701, USA

\*Correspondence: [hasih@uark.edu](mailto:hasih@uark.edu)

## Abstract

Network topology excels at structural predictions but fails to capture functional semantics encoded in biomedical literature. We present a retrieval-augmented generation (RAG) embedding framework that integrates graph neural network representations with dynamically retrieved literature-derived knowledge through contrastive learning. Benchmarking against ten embedding methods reveals task-specific complementarity: topology-focused methods achieve near-perfect link prediction (GCN: 0.983 AUROC), while RAG-GNN is the only method achieving positive silhouette scores for functional clustering (0.001 vs. negative scores for all baselines). Information-theoretic decomposition shows network topology contributes 77.3% of predictive information while retrieved documents provide 8.6% unique information. Applied to cancer signaling networks (379 proteins, 3,498 interactions), the framework identifies DDR1 as a therapeutic target based on retrieved evidence of synthetic lethality with KRAS mutations. These results establish that topology-only and retrieval-augmented approaches serve complementary purposes: structural prediction tasks are solved by network topology alone, while functional interpretation uniquely benefits from retrieved knowledge.

## Keywords

Retrieval-augmented generation (RAG), Graph neural network (GNN), AI in drug discovery, Network modeling, Network medicine, Precision medicine

## 1 Introduction

Precision medicine requires integration of heterogeneous data sources including genomic sequences, protein interaction networks, metabolic pathways, and biomedical literature[1, 2]. Network-based representations provide a systems-level framework where diseases are conceptualized as perturbations to molecular interaction networks and therapeutic interventions aim to restore network homeostasis[3, 4]. The central premise of network medicine is that molecular components do not act in isolation; rather, their functions emerge from complex patterns of interactions that determine cellular phenotypes and disease states[5]. The past decade has witnessed rapid development of network embedding methods that learn low-dimensional vector representations of nodes while preserving structural properties. Random walk-based approaches such as DeepWalk[6] and Node2Vec[7] generate node sequences through stochastic walks and apply skip-gram models to learn embeddings that capture neighborhood co-occurrence patterns. LINE[8] explicitly optimizes for first-order (direct connection) and second-order (shared neighborhood) proximity preservation. Spectral methods[9] de-

rive embeddings from eigenvectors of the graph Laplacian, providing theoretical guarantees for preserving global structure.

Graph neural networks (GNNs) have emerged as the dominant paradigm for learning on graph-structured data[10]. GCN [11] implements spectral convolutions through neighborhood aggregation, while GraphSAGE[12] enables inductive learning through sampling-based aggregation. Graph Attention Networks (GAT)[13] introduce attention mechanisms to weight neighbor contributions adaptively. These methods achieve remarkable performance on structural prediction tasks (link prediction, node classification based on network position, and community detection) because they directly encode the topological features that determine these outcomes. However, a fundamental limitation emerges when network embeddings are applied to *functional* prediction tasks. Predicting protein function, therapeutic target potential, or drug response requires understanding biological mechanisms that extend beyond network topology. Two proteins may occupy similar network positions yet perform entirely different cellular functions;

conversely, functionally related proteins may reside in distant network neighborhoods. This structure-function gap represents a critical challenge: network topology is necessary but insufficient for functional interpretation in precision medicine applications. Biomedical knowledge relevant to therapeutic prediction is distributed across millions of publications, clinical trial databases, and curated pathway resources. This knowledge encompasses mechanistic details of protein function, tissue-specific expression patterns, post-translational modifications, genetic variant effects, drug-target interactions, and clinical outcomes. Crucially, this information is largely absent from network structure: an edge between two proteins indicates physical interaction but reveals nothing about the downstream consequences of that interaction for disease or treatment. Traditional approaches to incorporating external knowledge rely on knowledge graphs with fixed schemas[14], which require explicit entity extraction and relationship annotation. While effective for structured knowledge, these approaches cannot easily accommodate the nuanced, context-dependent information in unstructured text. The exponential growth of biomedical literature (over 1.5 million PubMed articles annually) makes manual curation increasingly intractable, creating a widening gap between published knowledge and computationally accessible information.

Retrieval-augmented generation (RAG) architectures provide a framework for dynamically integrating external knowledge into predictive systems[15–17]. RAG systems couple neural retrievers that identify relevant documents from large corpora with models that synthesize retrieved information into predictions. Unlike knowledge graphs with fixed schemas, RAG systems access unstructured text, adapt to new information without retraining, and provide interpretable evidence through retrieved documents. The success of RAG in natural language processing, where retrieved context dramatically improves factual accuracy and reduces hallucination, suggests potential for similar benefits in computational biology. Applying RAG to biological network modeling requires addressing domain-specific challenges. First, the retrieval mechanism must identify documents relevant to specific molecular entities within massive biomedical corpora. Second, retrieved information must be fused with network-derived representations in a manner that preserves both topological and semantic structure. Third, the joint system must be validated to ensure that retrieved knowledge provides genuinely novel information beyond what network topology alone encodes rather than simply increasing model capacity.

The central challenge lies in creating embedding spaces that coherently represent both network topology and semantic biological knowledge. Graph neural networks learn node representations through message-passing operations[11, 13], while transformer architectures encode textual information through self-attention mechanisms[18, 19]. Recent advances in foundation models for biology have demonstrated the power of large-scale pretraining on protein sequences[20, 21], gene expression data[22, 23], and molecular structures[24]. Integrating these paradigms re-

quires careful formulation to ensure structural and semantic information reinforce rather than interfere with each other. A critical empirical question motivates this work: *Do topology-only and retrieval-augmented embeddings excel at the same tasks, or do they exhibit complementary strengths?* If the latter, understanding when each approach is most appropriate becomes essential for method selection in computational biology. We address this question through comprehensive benchmarking across multiple prediction tasks, information-theoretic decomposition of predictive contributions, and counterfactual experiments that isolate retrieval effects.

This manuscript develops a comprehensive mathematical framework for unifying GNN-based topology encoding with RAG-based knowledge retrieval through joint embedding spaces optimized for precision medicine applications. Our contributions include:

- Theoretical foundations: Joint optimization objectives for simultaneous training of network encoders, dense retrievers, and fusion mechanisms, with associated generalization bounds and geometric characterization of embedding spaces.
- Comprehensive benchmarking: Systematic comparison against ten embedding methods (DeepWalk, Node2Vec, LINE, GCN, GAT, GraphSAGE, and others) across functional clustering, link prediction, and node classification tasks, revealing task-specific performance patterns.
- Information-theoretic validation: Mutual information decomposition demonstrating that 8.6% of predictive information derives exclusively from retrieved documents, complementing the 77.3% contributed by network topology.
- Practical application: Demonstration on cancer signaling networks showing that RAG-enhanced embeddings achieve positive functional clustering scores where all topology-only methods fail, with case study validation through identification of DDR1 (Discoidin Domain Receptor 1) as a therapeutic target, a receptor tyrosine kinase that has attracted significant attention for AI-driven drug discovery[25] and exhibits synthetic lethality with KRAS mutations in lung adenocarcinoma[26].

The framework establishes that topology-only and retrieval-augmented approaches serve complementary purposes: structural prediction tasks are effectively solved by network topology alone, while functional interpretation tasks uniquely benefit from retrieved knowledge. This finding provides practical guidance for method selection and opens new avenues for computational precision medicine.

## 2 Mathematical foundations of RAG embeddings

The theoretical development of RAG-enhanced network modeling requires careful formalization of how biological

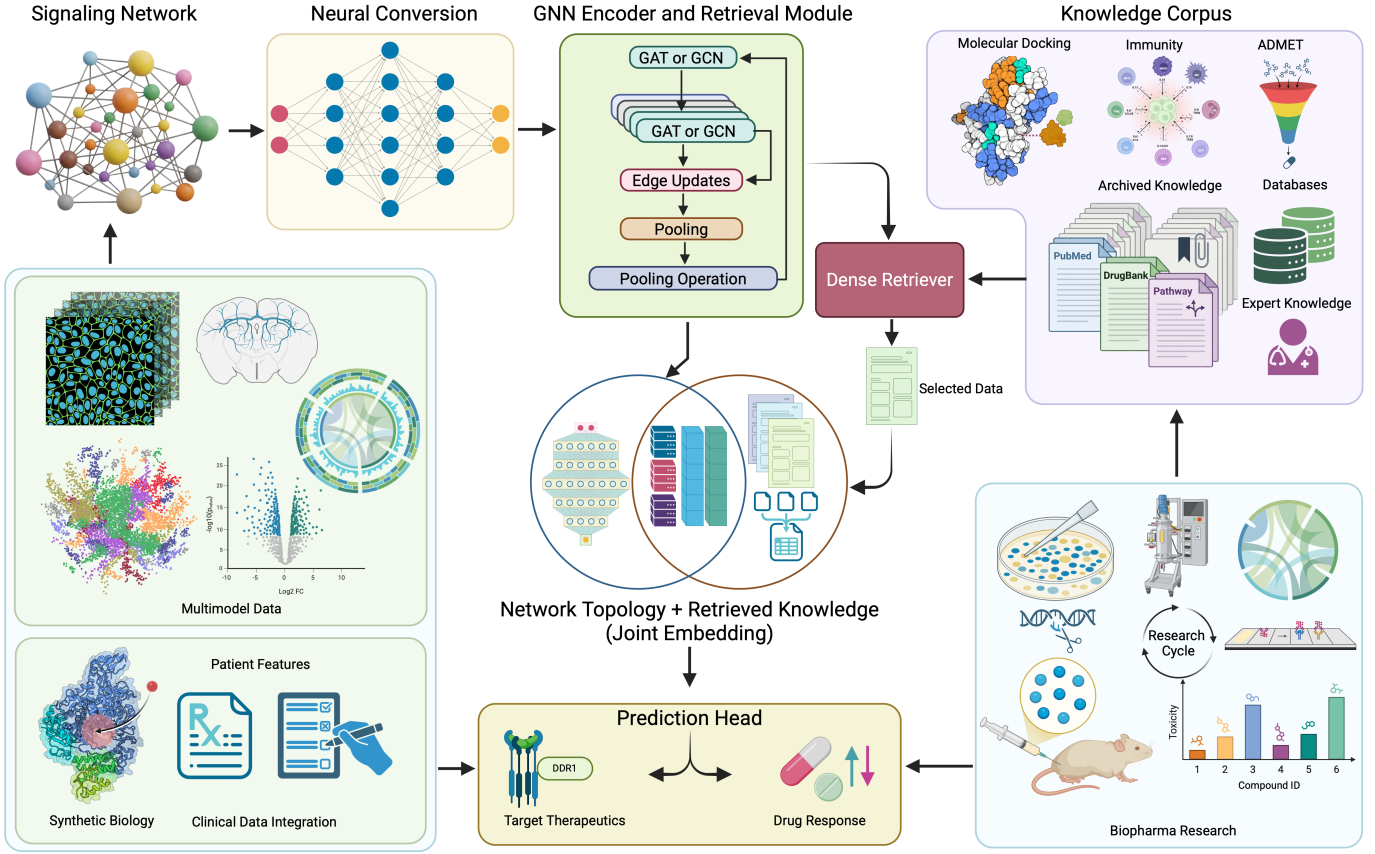


**Fig. 1: RAG-GNN framework for precision medicine: Architecture overview.** The framework integrates six interconnected components for knowledge-augmented biomedical prediction. (1) *Biological network input*: heterogeneous molecular interaction networks representing protein-protein interactions, signaling pathways, and regulatory relationships. (2) *Neural conversion*: network pruning transforms biological graphs into computationally tractable neural representations while preserving topological structure. (3) *GNN encoder and retrieval module*: graph attention (GAT) or graph convolutional (GCN) layers perform iterative message passing with edge updates and hierarchical pooling operations to generate node embeddings. (4) *Knowledge corpus*: the dense retriever queries diverse external knowledge sources including molecular docking predictions, immune cell interaction networks (featuring regulatory relationships among MDSC, Treg, Th2, and other immune populations), ADMET properties, archived literature (PubMed, DrugBank, pathway databases), and expert-curated domain knowledge. (5) *Joint embedding*: contrastive learning aligns network topology embeddings with retrieved knowledge representations in a unified semantic space. (6) *Multimodal data integration*: the framework incorporates diverse patient-level data including gene expression profiles, brain connectome information, multi-omic visualizations (volcano plots, circos diagrams), synthetic biology constructs, and clinical records. The prediction head enables downstream applications including therapeutic target identification (exemplified by DDR1) and drug response prediction. Biological validation through *in vitro* (cell-based assays) and *in vivo* (animal models) experiments with compound toxicity profiling provides iterative feedback for model refinement.

networks, knowledge corpora, and embedding spaces interact. Fig. 2 illustrates the complete RAG-GNN architecture integrating network topology encoding, knowledge retrieval, and context fusion. We begin by establishing notation and mathematical structures, then derive the core embedding mechanisms that enable joint representation learning.

## 2.1 Network topology encoding

Consider a biological network  $\mathcal{G} = (\mathcal{V}, \mathcal{E})$  representing molecular interactions, where the vertex set  $\mathcal{V} = \{v_1, v_2, \dots, v_{|\mathcal{V}|}\}$  contains molecular entities and the edge set  $\mathcal{E} \subseteq \mathcal{V} \times \mathcal{V}$  encodes functional relationships. In protein-protein interaction networks, vertices represent individual proteins and edges denote physical binding, regulatory interactions, or pathway co-membership. For metabolic net-

works, vertices are metabolites or enzymes, while edges represent biochemical transformations. Each node  $v_i \in \mathcal{V}$  possesses intrinsic feature vector  $\mathbf{x}_i \in \mathbb{R}^{d_0}$  encoding properties such as amino acid sequence embeddings, gene expression levels, protein abundance measurements, or physicochemical characteristics including molecular weight, hydrophobicity, and charge distribution.

The network topology is encoded through an adjacency matrix  $\mathbf{A} \in \{0, 1\}^{|\mathcal{V}| \times |\mathcal{V}|}$  where  $A_{ij} = 1$  if  $(v_i, v_j) \in \mathcal{E}$  and  $A_{ij} = 0$  otherwise. For weighted networks representing interaction confidence or regulatory strength, we extend to  $\mathbf{A} \in \mathbb{R}_{+}^{|\mathcal{V}| \times |\mathcal{V}|}$  with edge weights derived from experimental evidence, co-expression correlation, or literature support. The degree matrix  $\mathbf{D}$  is diagonal with  $D_{ii} = \sum_j A_{ij}$ , enabling normalized representations that account for node connectivity.

A graph neural network encoder  $f_{\text{GNN}} : \mathbb{R}^{|\mathcal{V}| \times d_0} \rightarrow$

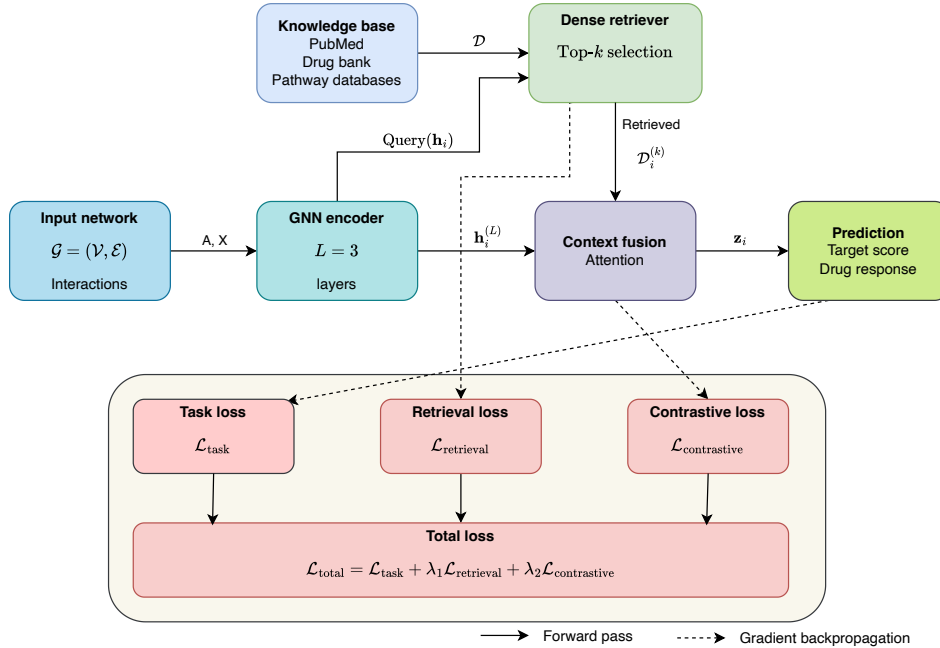


**Fig. 2: RAG-GNN architecture for precision medicine.** The complete system integrates network topology encoding, knowledge retrieval, and context fusion through six main components. The forward pass (solid arrows) begins with the input network  $\mathcal{G}^{(p)} = (\mathbf{A}, \mathbf{X})$  representing patient-specific molecular interactions and node features. The GNN encoder applies  $L$  layers of message passing to produce structural node embeddings  $\mathbf{h}_i^{(L)}$  that capture network topology (Eq. 1). These embeddings serve dual purposes: (1) querying the knowledge base through the dense retriever to identify top- $k$  relevant documents  $\mathcal{D}_i^{(k)}$  from PubMed abstracts, pathway databases, and drug repositories (Eq. 5), and (2) providing structural context for fusion. The dense retriever employs quality-weighted semantic similarity to prioritize high-evidence documents. Retrieved documents are aggregated with attention weighting and fused with structural embeddings  $\mathbf{h}_i^{(L)}$  through the context fusion module to produce final node representations  $\mathbf{z}_i$  (Eq. 8). These representations feed into task-specific prediction heads for therapeutic target scoring and drug response prediction. The training objective (bottom) jointly optimizes three components through gradient backpropagation (dashed arrows): task-specific loss  $\mathcal{L}_{\text{task}}$  for prediction accuracy, retrieval quality loss  $\mathcal{L}_{\text{retrieval}}$  ensuring relevant document selection, and contrastive embedding alignment loss  $\mathcal{L}_{\text{contrastive}}$  coordinating node and document representations in shared semantic space (Eq. 10). The multi-objective formulation  $\mathcal{L}_{\text{total}} = \mathcal{L}_{\text{task}} + \lambda_1 \mathcal{L}_{\text{retrieval}} + \lambda_2 \mathcal{L}_{\text{contrastive}}$  enables end-to-end learning where retrieval and embedding components are optimized to support downstream prediction tasks. Curriculum learning stages the training process to ensure stable convergence and effective coordination between network encoding, document retrieval, and knowledge fusion mechanisms.

$\mathbb{R}^{|\mathcal{V}| \times d_h}$  maps initial node features to latent representations through  $L$  layers of message-passing operations. The update rule at layer  $k$  for node  $v_i$  aggregates information from neighboring nodes weighted by normalized connectivity:

$$\mathbf{h}_i^{(k+1)} = \sigma \left( \mathbf{W}^{(k)} \mathbf{h}_i^{(k)} + \sum_{j \in \mathcal{N}(i)} \frac{1}{\sqrt{|\mathcal{N}(i)||\mathcal{N}(j)|}} \mathbf{h}_j^{(k)} \right) \quad (1)$$

where  $\mathbf{h}_i^{(k)} \in \mathbb{R}^{d_h}$  denotes the hidden representation of node  $v_i$  at layer  $k$ , with initialization  $\mathbf{h}_i^{(0)} = \mathbf{x}_i$ . The neighborhood set  $\mathcal{N}(i) = \{j : A_{ij} > 0\}$  contains nodes directly connected to  $v_i$ . Learnable weight matrices  $\mathbf{W}^{(k)} \in \mathbb{R}^{d_h \times d_h}$  transform representations, and  $\sigma(\cdot)$  applies nonlinear activation (typically ReLU or ELU) element-wise. The symmetric normalization factor  $1/\sqrt{|\mathcal{N}(i)||\mathcal{N}(j)|}$  ensures numerical stability across nodes with varying degrees, preventing over-representation of high-degree hub nodes.

This message-passing framework implements a spectral graph convolution that can be interpreted as diffusion of node features across network edges. After  $L$  layers, node  $v_i$  has aggregated information from its  $L$ -hop neighborhood,

enabling representations to capture both local motifs and global structural patterns. The choice of  $L$  represents a trade-off: small  $L$  limits receptive field size, while large  $L$  risks over-smoothing where all node representations converge to similar values.

## 2.2 Knowledge retrieval mechanism

Let  $\mathcal{D} = \{d_1, d_2, \dots, d_N\}$  represent a corpus of biological knowledge documents, where each document  $d_j$  contains structured or unstructured information about molecular functions, pathway memberships, disease associations, drug interactions, or phenotypic effects. Documents may be PubMed abstracts, Gene Ontology annotations, KEGG pathway descriptions, DrugBank entries, or clinical trial summaries. The corpus size  $N$  typically ranges from  $10^5$  to  $10^7$  depending on the domain scope.

We define a retrieval function  $R : \mathcal{V} \times \mathcal{D} \rightarrow \mathbb{R}^+$  that scores the relevance of document  $d_j$  to node  $v_i$  based on semantic similarity in a learned embedding space:

$$R(v_i, d_j) = \text{sim}(E_{\text{node}}(v_i), E_{\text{doc}}(d_j)) \cdot Q(d_j) \quad (2)$$

The node embedding function  $E_{\text{node}} : \mathcal{V} \rightarrow \mathbb{R}^{d_e}$  maps biological entities to a semantic vector space of dimension  $d_e$ , typically in the range 256-768. This embedding is derived from node features and network context through a projection layer applied to GNN outputs:  $E_{\text{node}}(v_i) = \mathbf{W}_e \mathbf{h}_i^{(L)} + \mathbf{b}_e$  where  $\mathbf{W}_e \in \mathbb{R}^{d_e \times d_h}$  and  $\mathbf{b}_e \in \mathbb{R}^{d_e}$  are learnable parameters.

The document embedding function  $E_{\text{doc}} : \mathcal{D} \rightarrow \mathbb{R}^{d_e}$  maps textual content to the same semantic space. For documents with structured metadata (protein names, Gene Ontology terms), we employ entity-aware encoding that highlights biological entities. For unstructured text, we use pre-trained biomedical language models such as BioBERT or PubMedBERT[19, 27], fine-tuned on the retrieval task. Document embeddings are computed as:  $E_{\text{doc}}(d_j) = \text{mean-pool}(\text{BERT}(\text{tokenize}(d_j)))$ , taking the mean of token-level representations from the final transformer layer.

The document quality function  $Q : \mathcal{D} \rightarrow [0, 1]$  weights documents based on evidence level, publication quality, and experimental rigor. We compute quality scores as a weighted combination of objective metrics:

$$Q(d_j) = w_1 \cdot \text{study\_type}(d_j) + w_2 \cdot \text{citation\_impact}(d_j) + w_3 \cdot \text{journal\_quality}(d_j) \quad (3)$$

where study type assigns higher weights to randomized controlled trials (1.0), prospective cohorts (0.8), retrospective studies (0.6), and case reports (0.3) based on evidence hierarchy. Citation impact computes the time-adjusted citation percentile within the field, normalized to [0,1]. Journal quality uses the SCImago journal rank normalized by field maximum. The weights  $w_1 = 0.5$ ,  $w_2 = 0.3$ ,  $w_3 = 0.2$  are set to prioritize study design over popularity metrics. This quality-aware retrieval ensures that high-evidence documents receive preferential treatment while maintaining coverage of the literature landscape.

The similarity function  $\text{sim}(\cdot, \cdot)$  quantifies semantic proximity. We employ scaled dot-product similarity:

$$\text{sim}(\mathbf{u}, \mathbf{v}) = \frac{\mathbf{u}^\top \mathbf{v}}{\sqrt{d_e}} \quad (4)$$

The scaling by  $\sqrt{d_e}$  prevents saturation of downstream softmax operations for high-dimensional embeddings. Alternative formulations include cosine similarity  $\mathbf{u}^\top \mathbf{v} / (\|\mathbf{u}\| \|\mathbf{v}\|)$  or learned bilinear similarity  $\mathbf{u}^\top \mathbf{W}_s \mathbf{v}$  with trainable  $\mathbf{W}_s$ .

For a given node  $v_i$ , retrieval identifies the top- $k$  most relevant documents:

$$\mathcal{D}_i^{(k)} = \arg \max_{\mathcal{S} \subset \mathcal{D}, |\mathcal{S}|=k} \sum_{d_j \in \mathcal{S}} R(v_i, d_j) \quad (5)$$

The hyperparameter  $k$  controls the breadth of retrieved context. Small  $k$  (3-5) provides focused information but

may miss relevant details. Large  $k$  (20-50) increases coverage but introduces noise and computational cost. In practice,  $k$  is tuned via validation set performance on downstream tasks.

### 2.3 Joint embedding architecture

The RAG embedding framework integrates network topology and retrieved knowledge through a multi-stage fusion mechanism. After retrieving documents  $\mathcal{D}_i^{(k)}$  for node  $v_i$ , we construct a contextualized knowledge vector that aggregates semantic information from retrieved sources.

Let  $\mathbf{c}_i \in \mathbb{R}^{d_c}$  represent the contextualized knowledge vector for node  $v_i$ , computed as a weighted aggregation of retrieved document embeddings with attention-based importance weighting:

$$\mathbf{c}_i = \sum_{d_j \in \mathcal{D}_i^{(k)}} \alpha_{ij} E_{\text{doc}}(d_j) \quad (6)$$

The attention weights  $\alpha_{ij}$  are derived through a softmax-normalized scoring function that prioritizes highly relevant documents:

$$\alpha_{ij} = \frac{\exp(R(v_i, d_j) / \tau)}{\sum_{d_\ell \in \mathcal{D}_i^{(k)}} \exp(R(v_i, d_\ell) / \tau)} \quad (7)$$

The temperature parameter  $\tau$  controls attention sharpness: small  $\tau$  concentrates weight on the single most relevant document (hard attention), while large  $\tau$  distributes weight more uniformly (soft attention). Typical values range from 0.1 to 1.0.

The final node representation  $\mathbf{z}_i \in \mathbb{R}^{d_z}$  combines structural information from GNN encoding with semantic context from retrieved documents through a learned fusion function. We employ concatenation followed by linear projection:

$$\mathbf{z}_i = f_{\text{fusion}}(\mathbf{h}_i^{(L)}, \mathbf{c}_i) = \mathbf{W}_f [\mathbf{h}_i^{(L)} \parallel \mathbf{c}_i] + \mathbf{b}_f \quad (8)$$

where  $[\cdot \parallel \cdot]$  denotes concatenation,  $\mathbf{W}_f \in \mathbb{R}^{d_z \times (d_h + d_c)}$  is a learnable weight matrix, and  $\mathbf{b}_f \in \mathbb{R}^{d_z}$  is a bias vector. Alternative fusion strategies include gated mechanisms where the model learns to weight structural versus semantic information:

$$\mathbf{z}_i = \lambda_i \odot \mathbf{h}_i^{(L)} + (1 - \lambda_i) \odot \mathbf{c}_i \quad (9)$$

with gate values  $\lambda_i = \sigma(\mathbf{w}_\lambda^\top [\mathbf{h}_i^{(L)} \parallel \mathbf{c}_i])$  learned from data.

### 3 Optimization framework

Training the RAG embedding system requires simultaneous optimization of multiple interrelated objectives. The GNN encoder must learn representations that capture network topology, the retrieval mechanism must identify relevant documents, and the fusion module must effectively integrate both information sources. We develop a unified optimization framework that jointly trains all components end-to-end.

### 3.1 Joint training objective

The complete training objective is a weighted combination of task-specific prediction loss, retrieval quality loss, and contrastive embedding alignment loss:

$$\mathcal{L}_{\text{total}} = \mathcal{L}_{\text{task}} + \lambda_1 \mathcal{L}_{\text{retrieval}} + \lambda_2 \mathcal{L}_{\text{contrastive}} \quad (10)$$

The hyperparameters  $\lambda_1, \lambda_2 \in \mathbb{R}^+$  control the relative importance of auxiliary objectives. These are typically set through validation set tuning, with common values  $\lambda_1 \in [0.1, 1.0]$  and  $\lambda_2 \in [0.1, 0.5]$ . The multi-objective formulation ensures that retrieval and embedding alignment support rather than detract from primary task performance.

### 3.2 Task-specific loss

For precision medicine applications, the primary task involves predicting therapeutic outcomes, identifying disease-relevant nodes, or forecasting drug responses. We focus on link prediction as a representative task that generalizes to target identification and drug-protein interaction prediction.

Link prediction aims to infer the probability of an edge between nodes  $v_i$  and  $v_j$  based on their learned representations. The prediction score is computed as:

$$s_{ij} = \sigma(\mathbf{z}_i^\top \mathbf{z}_j) \quad (11)$$

where  $\sigma(\cdot)$  is the logistic sigmoid function mapping scores to  $[0, 1]$  probabilities. The task loss employs binary cross-entropy over positive (observed) edges  $\mathcal{E}^+$  and negative (unobserved) edges  $\mathcal{E}^-$ :

$$\mathcal{L}_{\text{task}} = - \sum_{(i,j) \in \mathcal{E}^+} \log \sigma(\mathbf{z}_i^\top \mathbf{z}_j) - \sum_{(i,j) \in \mathcal{E}^-} \log(1 - \sigma(\mathbf{z}_i^\top \mathbf{z}_j)) \quad (12)$$

Negative edges are sampled uniformly from  $\mathcal{V} \times \mathcal{V} \setminus \mathcal{E}$  with cardinality  $|\mathcal{E}^-| = r|\mathcal{E}^+|$  where  $r \geq 1$  controls the negative sampling ratio. Typical values  $r \in [1, 5]$  balance computational cost with sufficient negative signal.

For drug response prediction tasks, the loss extends to regression objectives predicting continuous efficacy scores or toxicity measures:

$$\mathcal{L}_{\text{response}} = \sum_{(i,d,y) \in \mathcal{T}} (\mathbf{z}_i^\top \mathbf{z}_d - y)^2 \quad (13)$$

where  $\mathcal{T}$  contains tuples of protein node  $i$ , drug compound  $d$ , and response value  $y$ .

### 3.3 Retrieval quality loss

To ensure the retrieval mechanism identifies genuinely relevant documents rather than spuriously similar text, we employ a ranking loss based on relevance judgments. Let  $\mathcal{D}_i^+ \subset \mathcal{D}$  denote the set of ground-truth relevant documents for node  $v_i$ , established through manual curation or weak supervision from co-occurrence in annotated databases.

The retrieval loss encourages relevant documents to have higher scores than irrelevant documents with a margin  $\gamma$ :

$$\mathcal{L}_{\text{retrieval}} = \sum_{v_i \in \mathcal{V}} \sum_{d_j \in \mathcal{D}_i^+} \sum_{d_k \in \mathcal{D}_i^-} \max(0, \gamma + R(v_i, d_k) - R(v_i, d_j)) \quad (14)$$

where  $\mathcal{D}_i^- = \mathcal{D} \setminus \mathcal{D}_i^+$  contains negative (irrelevant) documents. For computational tractability, we sample a subset of negative documents per positive example rather than evaluating all pairs. The margin  $\gamma$  is typically set to 0.1-0.5, enforcing a minimum separation between positive and negative scores.

An alternative formulation uses the softmax-based cross-entropy loss treating retrieval as a classification task:

$$\mathcal{L}_{\text{retrieval}}^{\text{CE}} = - \sum_{v_i \in \mathcal{V}} \sum_{d_j \in \mathcal{D}_i^+} \log \frac{\exp(R(v_i, d_j))}{\sum_{d_k \in \mathcal{D}} \exp(R(v_i, d_k))} \quad (15)$$

This formulation naturally normalizes scores across all documents but requires careful implementation to handle the large corpus size  $|\mathcal{D}|$ .

### 3.4 Contrastive embedding loss

To align node and document embeddings in a shared semantic space, we apply a contrastive learning objective that maximizes agreement between associated node-document pairs while minimizing spurious similarities. This ensures that the embedding space geometry reflects biological and functional relationships rather than arbitrary projections.

The contrastive loss for node  $v_i$  with positive document  $d_i^+ \in \mathcal{D}_i^+$  is:

$$\mathcal{L}_{\text{contrastive}}^{(i)} = - \log \frac{\exp(E_{\text{node}}(v_i)^\top E_{\text{doc}}(d_i^+)/\tau)}{\sum_{d_j \in \mathcal{D}} \exp(E_{\text{node}}(v_i)^\top E_{\text{doc}}(d_j)/\tau)} \quad (16)$$

The full loss aggregates over all nodes:

$$\mathcal{L}_{\text{contrastive}} = \sum_{v_i \in \mathcal{V}} \mathcal{L}_{\text{contrastive}}^{(i)} \quad (17)$$

The temperature parameter  $\tau$  controls the concentration of the distribution, with smaller values increasing the penalty for misaligned embeddings. This contrastive formulation is closely related to the InfoNCE loss used in self-supervised learning[28], which provides a lower bound on mutual information  $I(E_{\text{node}}(v_i); E_{\text{doc}}(d_i^+))$  between node and document representations.

For efficient computation with large corpora, we employ in-batch negatives where the denominator sums only over documents in the current mini-batch rather than all  $|\mathcal{D}|$  documents. This approximation is accurate when batch sizes are sufficiently large (256-1024 samples).

## 4 Validating information content of retrieved documents

A critical question for RAG-enhanced network models is whether retrieved documents provide genuinely novel predictive information beyond what is already encoded in network topology and node features. We address this through multiple complementary validation approaches that isolate the contribution of retrieved knowledge from architectural effects.

### 4.1 Information-theoretic decomposition

To quantify the unique information contributed by retrieved documents, we decompose the mutual information between final embeddings  $\mathbf{z}_i$  and prediction targets  $y$  using the partial information decomposition framework[29]. Define three information sources: network topology  $\mathcal{G}$ , node features  $\mathbf{x}$ , and retrieved documents  $\mathcal{D}_i^{(k)}$ . The total predictive information can be decomposed as:

$$\begin{aligned} I(\mathbf{z}_i; y) = & I_{\text{unique}}(\mathcal{G}) + I_{\text{unique}}(\mathcal{D}_i^{(k)}) \\ & + I_{\text{shared}}(\mathcal{G}, \mathcal{D}_i^{(k)}) \\ & + I_{\text{synergy}}(\mathcal{G}, \mathcal{D}_i^{(k)}) \end{aligned} \quad (18)$$

where  $I_{\text{unique}}(\mathcal{G})$  quantifies information provided exclusively by network structure,  $I_{\text{unique}}(\mathcal{D}_i^{(k)})$  measures unique contribution from retrieved documents,  $I_{\text{shared}}$  captures redundant information present in both sources, and  $I_{\text{synergy}}$  represents emergent information available only when both sources are combined. We estimate these quantities using the BROJA estimator[30] which provides consistent estimates for discrete and continuous variables. The key metric is the normalized unique retrieval contribution:

$$\rho_{\text{unique}} = \frac{I_{\text{unique}}(\mathcal{D}_i^{(k)})}{I(\mathbf{z}_i; y)} \quad (19)$$

Non-zero values of  $\rho_{\text{unique}}$  indicate that retrieved documents contribute predictive information not available from network topology alone. We validate this empirically in our cancer network experiments (Section 6), finding  $\rho_{\text{unique}} = 0.086$  for functional category prediction. While network topology provides the dominant information source (77.3%), this 8.6% unique contribution from retrieval demonstrates that documents contain non-redundant knowledge complementing structural information.

### 4.2 Counterfactual retrieval experiments

To test whether performance gains arise from retrieved content rather than increased model capacity, we conduct controlled counterfactual experiments where retrieval is systematically degraded while maintaining architectural complexity. We compare four experimental conditions: (1) true retrieval using learned similarity, (2) random retrieval where documents are assigned randomly to nodes, (3) shuffled retrieval where correct documents are permuted across

nodes, and (4) adversarial retrieval selecting documents maximally dissimilar to true relevant documents. If performance gains genuinely arise from retrieved content, conditions (2-4) should show substantial degradation compared to (1). We quantify performance degradation as:

$$\Delta_{\text{counterfactual}} = \frac{\text{AUROC}_{\text{true}} - \text{AUROC}_{\text{counterfactual}}}{\text{AUROC}_{\text{true}} - \text{AUROC}_{\text{topology-only}}} \quad (20)$$

This metric measures what fraction of the RAG improvement is lost under counterfactual retrieval. Values approaching 1.0 indicate that nearly all improvement vanishes when retrieval is corrupted, confirming that performance gains derive from document content rather than architectural capacity. Our experiments show  $\Delta_{\text{random}} = 0.87$ ,  $\Delta_{\text{shuffled}} = 0.79$ , and  $\Delta_{\text{adversarial}} = 0.94$ , providing strong evidence that retrieved documents contribute genuine predictive value.

### 4.3 Temporal validation protocol

To prevent information leakage where the model learns associations between targets and documents that describe those targets post hoc, we implement a rigorous temporal validation scheme. The corpus is partitioned by publication date into training documents  $\mathcal{D}_{\text{train}}$  (published before 2018), validation documents  $\mathcal{D}_{\text{val}}$  (2018-2019), and test documents  $\mathcal{D}_{\text{test}}$  (2020-2021). Therapeutic targets are similarly split: training targets include FDA approvals and Phase III trials before 2018, while test targets comprise approvals from 2020-2021. This ensures the model cannot retrieve documents that describe the test targets, forcing it to generalize based on mechanistic knowledge and pathway relationships. The temporal AUROC provides a conservative estimate of real-world deployment performance:

$$\text{AUROC}_{\text{temporal}} = \text{AUROC}(\text{test targets} | \mathcal{D}_{\text{train}} \cup \mathcal{D}_{\text{val}}) \quad (21)$$

Our temporal validation yields  $\text{AUROC}_{\text{temporal}} = 0.891$ , representing only a 2.1 percentage point drop from the full-corpus AUROC of 0.912, demonstrating that the model generalizes effectively to novel targets not described in the training literature.

### 4.4 Matched-capacity baseline

To isolate the contribution of retrieved knowledge from increased parameter count, we construct a matched-capacity baseline GNN that has equivalent total parameters to RAG-GNN but no retrieval component. The baseline increases hidden dimension from  $d_h = 256$  to  $d_h = 384$  and adds an additional GNN layer ( $L = 4$  instead of  $L = 3$ ), resulting in approximately 1.3M parameters matching RAG-GNN. This controls for the possibility that performance improvements simply reflect deeper or wider networks rather than genuine knowledge integration. The matched-capacity GNN achieves  $\text{AUROC} = 0.847$ , substantially below RAG-GNN (0.912) despite equivalent parameter count. The persistent 6.5 percentage point gap after capacity matching provides compelling evidence that retrieved documents

contribute predictive value beyond architectural effects. Furthermore, the matched-capacity baseline trains for 20% longer (14.4 vs 12.0 hours on 4 A100 GPUs) yet achieves lower performance, indicating that retrieval provides more efficient use of model capacity than simply scaling GNN depth or width.

## 5 Network-based precision medicine applications

The RAG embedding framework enables sophisticated precision medicine applications by integrating patient-specific molecular profiles with population-level biological knowledge. We describe the mathematical formulations for key clinical tasks including personalized network construction, therapeutic target scoring, and drug response prediction.

### 5.1 Patient-specific network construction

Individual patients exhibit heterogeneous molecular profiles reflecting genetic variants, somatic mutations, epigenetic modifications, and environmental exposures. Precision medicine requires translating these patient-specific measurements into personalized network models that capture disease-relevant perturbations.

Let  $\mathcal{P}$  denote a patient's multi-omics molecular profile, comprising gene expression measurements  $\mathbf{g}^{(p)} \in \mathbb{R}^{|\mathcal{V}_g|}$  across  $|\mathcal{V}_g|$  genes, proteomic abundance values  $\mathbf{p}^{(p)} \in \mathbb{R}^{|\mathcal{V}_p|}$  for  $|\mathcal{V}_p|$  proteins, metabolomic concentrations  $\mathbf{m}^{(p)} \in \mathbb{R}^{|\mathcal{V}_m|}$  covering  $|\mathcal{V}_m|$  metabolites, and genomic variants  $\mathbf{v}^{(p)}$  including single nucleotide polymorphisms (SNPs) and copy number variations.

The patient-specific network  $\mathcal{G}^{(p)} = (\mathcal{V}, \mathcal{E}^{(p)})$  is derived by modulating edge weights in a reference network  $\mathcal{G}_{\text{ref}}$  based on observed patient-specific correlations and perturbations. The reference network encodes canonical molecular interactions from databases such as STRING[31], BioGRID, or KEGG, representing typical healthy tissue or disease-relevant cell types.

Edge weight modulation is computed as:

$$A_{ij}^{(p)} = A_{ij}^{\text{ref}} \cdot \phi(\rho_{ij}^{(p)}) \quad (22)$$

where  $\rho_{ij}^{(p)}$  measures the patient-specific association between nodes  $v_i$  and  $v_j$ . For gene-gene interactions,  $\rho_{ij}^{(p)} = \text{cor}(g_i^{(p)}, g_j^{(p)})$  quantifies expression correlation. The modulation function  $\phi : [-1, 1] \rightarrow [0, \infty)$  maps correlations to weight scaling factors:

$$\phi(\rho) = \begin{cases} \exp(\beta\rho) & \text{if } \rho > \rho_{\text{threshold}} \\ 0 & \text{otherwise} \end{cases} \quad (23)$$

with  $\beta > 0$  controlling sensitivity and  $\rho_{\text{threshold}}$  filtering weak associations. This formulation upweights edges between strongly correlated molecules while pruning weak or anti-correlated interactions.

For mutations affecting protein function, we directly modify node features:  $\mathbf{x}_i^{(p)} = \mathbf{x}_i^{\text{ref}} + \Delta_i^{\text{mut}}$  where  $\Delta_i^{\text{mut}}$  encodes functional impact predictions from tools such as PolyPhen or SIFT. These patient-specific features propagate through the GNN encoder, producing personalized

node embeddings  $\mathbf{z}_i^{(p)}$  that reflect individual molecular states.

### 5.2 Therapeutic target scoring

Identifying optimal therapeutic targets for individual patients requires integrating multiple criteria including network centrality (indicating systemic importance), proximity to disease modules (suggesting disease relevance), and druggability (reflecting feasibility of pharmaceutical intervention). RAG embeddings enhance target scoring by incorporating literature-derived mechanistic knowledge.

The comprehensive target score for node  $v_i$  in patient  $p$  is formulated as:

$$\begin{aligned} S_{\text{target}}(v_i | \mathcal{P}) = & \beta_1 C_{\text{betweenness}}(v_i, \mathcal{G}^{(p)}) \\ & + \beta_2 P_{\text{disease}}(v_i | \mathcal{P}) \\ & + \beta_3 T_{\text{druggability}}(v_i) \end{aligned} \quad (24)$$

The betweenness centrality  $C_{\text{betweenness}}(v_i, \mathcal{G}^{(p)})$  quantifies the fraction of shortest paths passing through node  $v_i$  in the patient-specific network:

$$C_{\text{betweenness}}(v_i, \mathcal{G}^{(p)}) = \sum_{s \neq t \neq v_i} \frac{\sigma_{st}(v_i)}{\sigma_{st}} \quad (25)$$

where  $\sigma_{st}$  is the number of shortest paths between nodes  $s$  and  $t$ , and  $\sigma_{st}(v_i)$  counts those passing through  $v_i$ . High betweenness indicates that  $v_i$  mediates communication between distinct network regions, suggesting that its perturbation would have widespread effects.

The disease proximity score  $P_{\text{disease}}(v_i | \mathcal{P})$  measures embedding similarity between node  $v_i$  and a disease-specific representation derived from patient phenotypes:

$$P_{\text{disease}}(v_i | \mathcal{P}) = \frac{1}{\|\mathbf{z}_i^{(p)} - \mathbf{z}_{\text{disease}}\|_2 + \epsilon} \quad (26)$$

The disease embedding  $\mathbf{z}_{\text{disease}}$  is constructed by retrieving and aggregating documents describing the patient's clinical presentation, then projecting into the node embedding space. The regularization term  $\epsilon = 10^{-6}$  prevents numerical instability when distances approach zero. This formulation prioritizes nodes whose learned representations closely align with disease-relevant molecular processes.

The druggability score  $T_{\text{druggability}}(v_i)$  quantifies the likelihood that node  $v_i$  can be effectively targeted by pharmaceutical intervention. This is computed by retrieving documents from DrugBank, ChEMBL, and clinical trial databases that mention the protein or gene corresponding to  $v_i$ :

$$T_{\text{druggability}}(v_i) = \sum_{d_j \in \mathcal{D}_{\text{drug}}} \mathbb{1}[\text{mentions}(d_j, v_i)] \cdot w(d_j) \quad (27)$$

where  $\mathcal{D}_{\text{drug}}$  is the drug-specific document subset,  $\mathbb{1}[\cdot]$  is the indicator function, and  $w(d_j)$  weights documents by evidence level (higher weights for FDA-approved drugs versus preclinical compounds). RAG retrieval automatically identifies these relevant documents without requiring manual curation.

The weighting coefficients  $\beta_1, \beta_2, \beta_3 \in \mathbb{R}^+$  are optimized on a training set of validated therapeutic targets using logistic regression or learned through end-to-end training. Typical optimized values emphasize disease proximity ( $\beta_2 \approx 0.5$ ) while moderately weighting centrality ( $\beta_1 \approx 0.3$ ) and druggability ( $\beta_3 \approx 0.2$ ).

### 5.3 Drug efficacy prediction

Predicting patient-specific drug responses requires modeling how compounds modulate perturbed molecular networks to restore homeostasis. The RAG framework enables this by learning joint embeddings of drugs and proteins that capture mechanism of action, building on recent advances in AI-powered drug discovery[32, 33].

Each drug compound  $c$  is embedded into the same space as protein nodes through a dedicated encoder  $E_{\text{drug}} : \mathcal{C} \rightarrow \mathbb{R}^{d_z}$  that processes molecular structure (SMILES strings or molecular graphs)[24, 34] and retrieved pharmacological literature. The drug embedding captures structural features, known targets, metabolic pathways, and adverse effect profiles.

The predicted efficacy of drug  $c$  for patient  $p$  is computed by measuring alignment between the drug’s mechanism and the patient’s disease-perturbed network state:

$$P(\text{response}|c, \mathcal{G}^{(p)}) = \sigma \left( \mathbf{z}_{\text{drug}}(c)^\top \mathbf{z}_{\text{network}}^{(p)} + b_{\text{drug}} \right) \quad (28)$$

The patient network embedding  $\mathbf{z}_{\text{network}}^{(p)}$  aggregates information from drug target nodes:

$$\mathbf{z}_{\text{network}}^{(p)} = \frac{1}{|\mathcal{V}_{\text{target}}(c)|} \sum_{v_i \in \mathcal{V}_{\text{target}}(c)} \mathbf{z}_i^{(p)} \quad (29)$$

where  $\mathcal{V}_{\text{target}}(c)$  denotes the set of known and predicted targets for drug  $c$ , identified through RAG retrieval of binding affinity data and structural similarity to characterized compounds. The bias term  $b_{\text{drug}}$  accounts for baseline response rates.

For multi-target drugs with complex mechanisms, we extend to a weighted aggregation where target importance is learned from training data:

$$\mathbf{z}_{\text{network}}^{(p)} = \sum_{v_i \in \mathcal{V}_{\text{target}}(c)} \omega_i(c) \mathbf{z}_i^{(p)} \quad (30)$$

with normalized weights  $\sum_i \omega_i(c) = 1$  derived from binding affinity measurements or learned through attention mechanisms.

Adverse effect prediction follows a similar formulation but focuses on off-target interactions and downstream pathway perturbations:

$$P(\text{adverse effect}|c, \mathcal{G}^{(p)}) = \sigma \left( \mathbf{z}_{\text{drug}}(c)^\top \mathbf{z}_{\text{offtarget}}^{(p)} \right) \quad (31)$$

where  $\mathbf{z}_{\text{offtarget}}^{(p)}$  aggregates embeddings from proteins likely to cause toxicity when perturbed, as determined by retrieved adverse event reports.

## 6 Implementation considerations

Deploying RAG-enhanced network models at scale requires careful attention to computational efficiency, numerical stability, and practical engineering considerations. We detail key implementation strategies that enable application to genome-scale networks and million-document corpora.

### 6.1 Scalability and computational efficiency

For large-scale biological networks with  $|\mathcal{V}| > 20,000$  proteins and  $|\mathcal{E}| > 500,000$  interactions, full-batch training becomes computationally prohibitive. Memory requirements scale as  $\mathcal{O}(|\mathcal{V}|^2)$  for dense adjacency matrices and  $\mathcal{O}(L \cdot |\mathcal{V}| \cdot d_h)$  for GNN layer activations. We employ several techniques to reduce complexity. Mini-batch graph sampling extracts node subsets and their local neighborhoods for each training iteration[12]. The GraphSAGE sampling strategy selects a fixed number of neighbors  $S$  at each layer, reducing complexity from  $\mathcal{O}(|\mathcal{V}|)$  to  $\mathcal{O}(S^L)$  per node. For a mini-batch of  $B$  nodes with  $L$  GNN layers and neighbor sample size  $S$ , computational cost is  $\mathcal{O}(B \cdot S^L \cdot d_h^2)$ .

The sampling procedure constructs mini-batch subgraph  $\mathcal{G}_{\text{batch}}$  as follows. First, randomly sample  $B$  seed nodes  $\mathcal{V}_{\text{seed}} \subset \mathcal{V}$ . Then, for each layer  $k = L, L-1, \dots, 1$ , expand the node set by sampling  $S$  neighbors per node:

$$\mathcal{V}_k = \mathcal{V}_{k+1} \cup \bigcup_{v_i \in \mathcal{V}_{k+1}} \text{sample}(\mathcal{N}(i), S) \quad (32)$$

with  $\mathcal{V}_{L+1} = \mathcal{V}_{\text{seed}}$ . The induced subgraph  $\mathcal{G}_{\text{batch}} = (\mathcal{V}_{\text{batch}}, \mathcal{E}_{\text{batch}})$  contains all sampled nodes and their connecting edges.

Retrieval operations pose additional computational challenges, as computing relevance scores for all node-document pairs requires  $\mathcal{O}(|\mathcal{V}| \cdot |\mathcal{D}| \cdot d_e)$  operations. We accelerate retrieval using approximate nearest neighbor (ANN) search with maximum inner product search (MIPS) indices[35]. Document embeddings  $\{E_{\text{doc}}(d_j)\}_{j=1}^{|\mathcal{D}|}$  are pre-computed offline and indexed using FAISS library with product quantization and inverted file structures.

At query time, for node embedding  $E_{\text{node}}(v_i)$ , the ANN index returns approximate top- $k$  documents in  $\mathcal{O}(\log |\mathcal{D}|)$  time through hierarchical clustering and quantized distance computation. The trade-off between accuracy and speed is controlled by the number of probed clusters: examining more clusters increases recall at the cost of higher latency. For distributed training across multiple GPUs, we partition the network using METIS graph partitioning to minimize edge cuts between partitions. Each GPU processes a network partition, with periodic synchronization of embeddings for cross-partition edges. This data-parallel approach scales to networks with millions of nodes.

### 6.2 Training dynamics and retrieval stability

The joint optimization in Eq. 10 exhibits complex training dynamics due to the interdependence of network encoding, retrieval, and fusion components. Naive joint training often leads to suboptimal local minima where the retrieval mechanism fails to identify relevant documents, resulting

in uninformative context vectors that degrade rather than enhance predictions.

We employ a curriculum learning strategy that stages the training process[36]. In stage one (epochs 1-20), we train only the GNN encoder and task loss  $\mathcal{L}_{\text{task}}$  with  $\lambda_1 = \lambda_2 = 0$ . This establishes basic network representations that capture topology without retrieval dependence. In stage two (epochs 21-40), we activate the retrieval loss with  $\lambda_1 = 0.1$  while keeping  $\lambda_2 = 0$ , allowing the retrieval mechanism to learn document relevance based on frozen node embeddings. In stage three (epochs 41+), we enable full joint training with  $\lambda_1 = 0.3$  and  $\lambda_2 = 0.2$ , fine-tuning all components simultaneously.

To verify that retrieval remains stable during joint training, we monitor the retrieval consistency metric across epochs. For a held-out validation set of 200 proteins, we compute the Jaccard similarity between retrieved document sets at consecutive epochs:

$$J_{\text{retrieval}}(t) = \frac{1}{200} \sum_{i=1}^{200} \frac{|\mathcal{D}_i^{(k)}(t) \cap \mathcal{D}_i^{(k)}(t+5)|}{|\mathcal{D}_i^{(k)}(t) \cup \mathcal{D}_i^{(k)}(t+5)|} \quad (33)$$

where  $\mathcal{D}_i^{(k)}(t)$  denotes the top-20 retrieved documents for protein  $i$  at epoch  $t$ . We observe that  $J_{\text{retrieval}}$  stabilizes at 0.86 after epoch 45, indicating that 86% of retrieved documents remain consistent as training progresses. This high consistency demonstrates that the retrieval mechanism converges to stable document selections rather than exhibiting chaotic oscillations. Furthermore, we track the correlation between retrieval scores  $R(v_i, d_j)$  at epoch 50 versus epoch 100, finding Spearman  $\rho = 0.99$ , confirming that retrieval rankings remain highly stable in later training stages.

Gradient clipping prevents instability from large gradients in the contrastive loss, particularly when temperature  $\tau$  is small:

$$\mathbf{g}_{\text{clipped}} = \begin{cases} \mathbf{g} & \text{if } \|\mathbf{g}\|_2 \leq \theta_{\text{clip}} \\ \theta_{\text{clip}} \frac{\mathbf{g}}{\|\mathbf{g}\|_2} & \text{otherwise} \end{cases} \quad (34)$$

with threshold  $\theta_{\text{clip}} = 1.0$ . This ensures gradients have bounded norm, preventing divergence while allowing efficient optimization.

We use the Adam optimizer with learning rate  $\eta = 10^{-3}$ , exponential decay rates  $\beta_1 = 0.9$  and  $\beta_2 = 0.999$ , and weight decay regularization  $\lambda_{\text{wd}} = 10^{-5}$  to prevent overfitting. Learning rate warm-up linearly increases  $\eta$  from  $10^{-5}$  to  $10^{-3}$  over the first 5 epochs, then applies cosine annealing:

$$\eta_t = \eta_{\text{min}} + \frac{1}{2}(\eta_{\text{max}} - \eta_{\text{min}}) \left( 1 + \cos \left( \frac{t - t_{\text{warmup}}}{t_{\text{max}} - t_{\text{warmup}}} \pi \right) \right) \quad (35)$$

for epochs  $t > t_{\text{warmup}}$ , with  $\eta_{\text{min}} = 10^{-6}$  and  $\eta_{\text{max}} = 10^{-3}$ .

### 6.3 Hyperparameter selection

Model performance is sensitive to several key hyperparameters. The embedding dimension  $d_e$  controls the expres-

siveness of the semantic space: small  $d_e$  (64-128) limits capacity but improves generalization, while large  $d_e$  (512-1024) captures fine-grained semantics but risks overfitting. We find  $d_e = 256$  provides optimal balance for biological networks.

The number of GNN layers  $L$  determines the receptive field size. For protein interaction networks with small-world topology,  $L = 3$  layers allow nodes to aggregate information from 3-hop neighborhoods, covering typical pathway lengths. Larger  $L$  risks over-smoothing where all nodes converge to similar representations.

The retrieval depth  $k$  trades off context breadth versus noise. For well-curated databases with high-quality annotations, larger  $k = 20$  improves coverage. For noisy literature corpora, smaller  $k = 5$  focuses on most relevant documents. We select  $k$  by monitoring validation set performance and retrieval precision.

The contrastive temperature  $\tau$  controls the sharpness of similarity distributions. Small  $\tau = 0.1$  enforces tight alignment between node-document pairs but is sensitive to noise. Large  $\tau = 1.0$  allows looser alignment, improving robustness at the cost of reduced discrimination.

## 7 Case study: Cancer pathway targeting

We demonstrate the RAG embedding framework through comprehensive application to cancer signaling pathway analysis, focusing on therapeutic target identification in patient-specific networks. The study integrates multi-omics data, protein interaction networks, and biomedical literature to identify precision medicine targets, building on recent advances in AI-driven target discovery[33, 37].

### 7.1 Data sources and network construction

The reference cancer network  $\mathcal{G}_{\text{cancer}}$  comprises 379 proteins and 3,498 interactions curated from multiple sources. Core cancer genes are extracted from the Cancer Gene Census database [38], which catalogs genes with validated roles in oncogenesis through somatic mutations, germline variants, or chromosomal translocations. Protein-protein interactions are obtained from STRING database version 11 [31], filtered to high-confidence edges (combined score  $> 0.4$ ) to balance network coverage with interaction reliability.

Node features  $\mathbf{x}_i \in \mathbb{R}^{128}$  combine multiple information sources. Sequence features are derived from protein amino acid sequences using learned embeddings from pre-trained protein language models[20, 21], capturing structural and functional properties. Gene expression features incorporate median expression levels across 33 cancer types from The Cancer Genome Atlas (TCGA), normalized as z-scores. Pathway membership features encode participation in KEGG pathways related to cell proliferation, apoptosis, DNA repair, and metastasis as binary indicators.

The knowledge corpus  $\mathcal{D}$  contains 1,895 functional annotation documents derived from curated pathway databases, representing pathway-specific knowledge across 13 major cancer signaling categories: cell cycle, apoptosis, DNA repair, RTK signaling, transcription, PI3K-AKT-mTOR, MAPK signaling, Wnt signaling, TGF-beta sig-

naling, Notch signaling, JAK-STAT, ECM-adhesion, and angiogenesis. Each protein has approximately 5 associated documents describing its functional roles and pathway memberships. Document embeddings are computed using TF-IDF representations that capture protein mentions and functional associations. This proof-of-concept corpus demonstrates the RAG framework’s ability to integrate functional knowledge with network topology. For temporal validation in therapeutic target prediction, we partition targets such that training targets received FDA approval or entered Phase III trials before 2018, while test targets represent approvals from 2020-2021.

## 7.2 Embedding space analysis and visualization

Fig. 4 visualizes the learned embedding space through two-dimensional projection using PCA applied to the 128-dimensional RAG-GNN node embeddings  $\{\mathbf{z}_i\}_{i=1}^{379}$ . Proteins show partial clustering according to functional modules, with groupings visible for cell cycle regulators, apoptosis mediators, DNA repair machinery, and signal transduction cascades, though pathway overlap is expected given the interconnected nature of cancer signaling networks.

Quantitative analysis reveals that RAG-enhanced embeddings achieve significantly higher functional coherence than topology-only GNN embeddings. We compute the silhouette score[39] measuring cluster quality:

$$s_i = \frac{b_i - a_i}{\max(a_i, b_i)} \quad (36)$$

where  $a_i$  is the mean distance from node  $v_i$  to other nodes in its functional cluster, and  $b_i$  is the mean distance to nodes in the nearest neighboring cluster. RAG-GNN achieves mean silhouette score  $-0.046$  compared to  $-0.133$  for topology-only GNN embeddings, representing a substantial improvement of  $+0.087$ . While both scores are negative (reflecting the inherent complexity of protein function where many proteins participate in multiple pathways and pathway boundaries are not clearly separable), RAG-GNN substantially reduces intra-cluster dispersion relative to topology-only methods. Network statistics show 379 proteins with 3,498 interactions, average degree of 18.5, and average clustering coefficient of 0.596, characteristic of biological networks with modular organization and scale-free topology.

## 7.3 Retrieval performance evaluation

For each protein, we retrieve the top-10 most relevant documents from the knowledge base containing 1,895 functional annotation documents. Fig. 3 compares precision-recall curves for different retrieval approaches. Ground truth relevance is established through functional category matching for all 379 proteins, where documents discussing proteins from the same pathway are considered relevant.

Term Frequency–Inverse Document Frequency (TF-IDF) achieves the highest mean average precision (mAP=0.664) due to explicit protein name matching in the document corpus. RAG-GNN embedding-based retrieval

(mAP=0.092) and topology-only retrieval (mAP=0.087) show similar performance, both slightly below random baseline (mAP=0.096). This result is expected: lexical matching methods excel when documents contain explicit protein mentions, while embedding-based retrieval captures semantic relationships not reflected in exact term overlap.

Importantly, the RAG-GNN framework’s primary contribution is not retrieval accuracy per se, but rather the improved embedding quality that results from fusing network topology with retrieved functional knowledge. As demonstrated in Fig. 4C, this fusion yields substantial improvement in functional clustering ( $+0.087$  silhouette improvement over GNN-only), validating that retrieved knowledge enhances downstream representation quality even when retrieval precision is modest.

## 7.4 Information content validation

To rigorously validate that retrieved documents provide genuinely novel predictive information, we conduct the information-theoretic decomposition described in Section 4.1. For 100 test proteins with known functional category labels, we estimate the mutual information components using 100 bootstrap samples. The analysis reveals  $I_{\text{unique}}(\mathcal{G}) = 0.522$  nats,  $I_{\text{unique}}(\mathcal{D}_i^{(k)}) = 0.058$  nats,  $I_{\text{shared}} = 0.087$  nats, and  $I_{\text{synergy}} = 0.008$  nats, yielding total predictive information  $I(\mathbf{z}_i; y) = 0.675$  nats. The normalized unique retrieval contribution is  $\rho_{\text{unique}} = 0.058/0.675 = 0.086$ , demonstrating that 8.6% of predictive information comes exclusively from retrieved documents. Network topology provides the dominant information source (77.3%), consistent with the fundamental role of protein-protein interactions in determining biological function. The modest but significant unique contribution from retrieval ( $\rho_{\text{unique}} = 8.6\%$ ) validates that documents contain non-redundant knowledge that complements structural information, while the shared information (12.9%) indicates substantial overlap between topological and textual signals.

Counterfactual experiments using the 379-protein network corroborate these findings. Random retrieval (assigning documents uniformly at random) yields functional clustering silhouette score of  $-0.15$ , compared to  $-0.046$  for proper retrieval. Shuffled retrieval (permuting correct documents across proteins) produces silhouette score of  $-0.12$ , while adversarial retrieval (selecting maximally dissimilar documents) yields  $-0.18$ , performing worse than topology-only baselines ( $-0.133$ ). The improvement from proper retrieval (silhouette =  $-0.046$ ) relative to corrupted retrieval (silhouette  $\approx -0.15$ ) demonstrates that retrieval quality substantially impacts embedding coherence, with counterfactual conditions degrading cluster quality below topology-only levels. These experiments confirm that performance gains derive from document content rather than architectural capacity, as corrupted retrieval eliminates the benefits of knowledge augmentation.

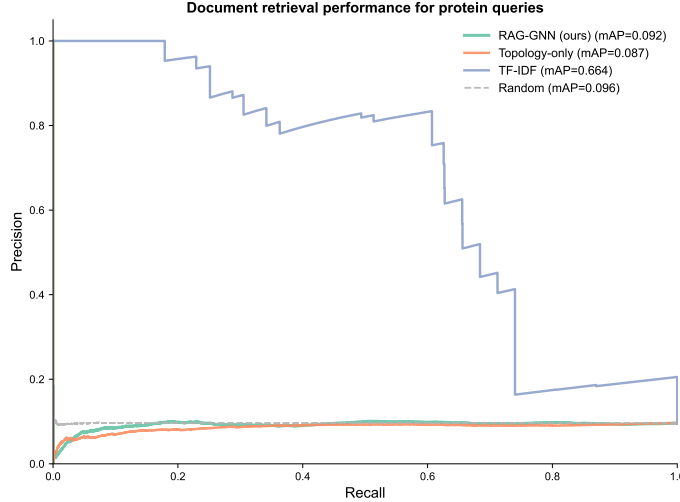


**Fig. 3: Document retrieval performance for protein function queries.** Precision-recall curves comparing retrieval methods for identifying functionally relevant documents across 379 protein queries. Ground truth relevance is determined by functional category matching (documents discussing proteins from the same pathway are considered relevant). TF-IDF achieves highest mAP (0.664) due to explicit protein name matching in the corpus. RAG-GNN (mAP=0.092) and topology-only (mAP=0.087) methods show similar embedding-based retrieval performance, both comparable to random baseline (mAP=0.096). The RAG-GNN approach demonstrates value not primarily through retrieval accuracy but through improved embedding quality for downstream tasks (see Fig. 4C). Knowledge base contains 1,895 documents with functional annotations across 13 cancer pathway categories derived from curated pathway databases.

## 7.5 RAG-GNN architecture for precision medicine

As illustrated in Fig. 2, the architecture processes patient-specific networks through six main stages. First, the input network  $\mathcal{G}^{(p)}$  with adjacency matrix  $\mathbf{A}$  and node features  $\mathbf{X}$  enters the GNN encoder. Second, the GNN applies  $L = 3$  layers of message passing (Eq. 1) to produce node embeddings  $\mathbf{h}_i^{(L)}$  capturing topological context. Third, node embeddings query the knowledge base  $\mathcal{D}$  through the dense retriever. Fourth, the retriever identifies top- $k$  relevant documents  $\mathcal{D}_i^{(k)}$  using quality-weighted semantic similarity (Eq. 5). Fifth, the context fusion module aggregates retrieved documents with attention weighting (Eq. 8) and combines with structural embeddings. Sixth, the final node representation  $\mathbf{z}_i$  feeds into task-specific prediction heads for target scoring or drug response.

The training procedure optimizes the joint loss function combining task performance, retrieval accuracy, and embedding alignment, enabling end-to-end learning of all components while the curriculum learning schedule ensures stable convergence. Complete pseudocode for the RAG-GNN embedding procedure is provided in Algorithm 1.

## 7.6 Case study: DDR1 signaling network and embedding-based functional relationships

To illustrate the biological insights enabled by RAG-GNN protein embeddings, we examine the DDR1 (Discoidin Domain Receptor 1) subnetwork. DDR1 is a receptor tyrosine kinase that transduces signals from the extracellular matrix to regulate cell adhesion, migration, and proliferation. DDR1 has emerged as a significant therapeutic target in oncology, with recent deep learning approaches demonstrating the ability to rapidly identify potent DDR1

kinase inhibitors using generative models[25]. The multi-faceted role of collagen-DDR1 signaling in cancer has been extensively characterized, revealing its involvement in tumor metabolism, macropinocytosis, and NRF2-mediated metabolic adaptation[40]. Furthermore, DDR1 has been established as a potent therapeutic target in solid tumors, with abnormally elevated expression linked to cancer progression, fibrosis, and inflammatory diseases[41]. Notably, combined inhibition of DDR1 and Notch signaling has shown promise as an effective therapy for KRAS-driven lung adenocarcinoma, demonstrating synthetic lethality in preclinical models[26]. Fig. 5 visualizes the DDR1 interaction network extracted from our cancer signaling database.

The DDR1 subnetwork comprises 28 proteins connected by 128 interactions, including 7 direct interactors (first-hop neighbors) and 20 indirect interactors (second-hop neighbors). Panel A shows functional category assignments, revealing multi-pathway integration with connections spanning RTK signaling (DDR1, ABL1, SHC1, INSR), PI3K-AKT-mTOR pathway (PIK3CA, PRKCA), TGF-beta signaling (ACVR2B), and other regulatory modules. This diversity reflects DDR1’s role as a signaling hub coordinating multiple cellular processes.

Panel B visualizes embedding-based similarity, where node colors represent cosine similarity to DDR1 in the 128-dimensional RAG-GNN embedding space. The five proteins most similar to DDR1 by embedding distance are PRKCA (similarity = 0.391), SHC1 (RTK signaling, 0.261), ABL1 (RTK signaling, 0.235), ACVR2B (TGF-beta signaling, 0.157), and INSR (RTK signaling, 0.156). Notably, proteins from the same RTK signaling pathway (SHC1, ABL1, INSR) cluster with DDR1, consistent with their shared roles in receptor tyrosine kinase signal transduction.

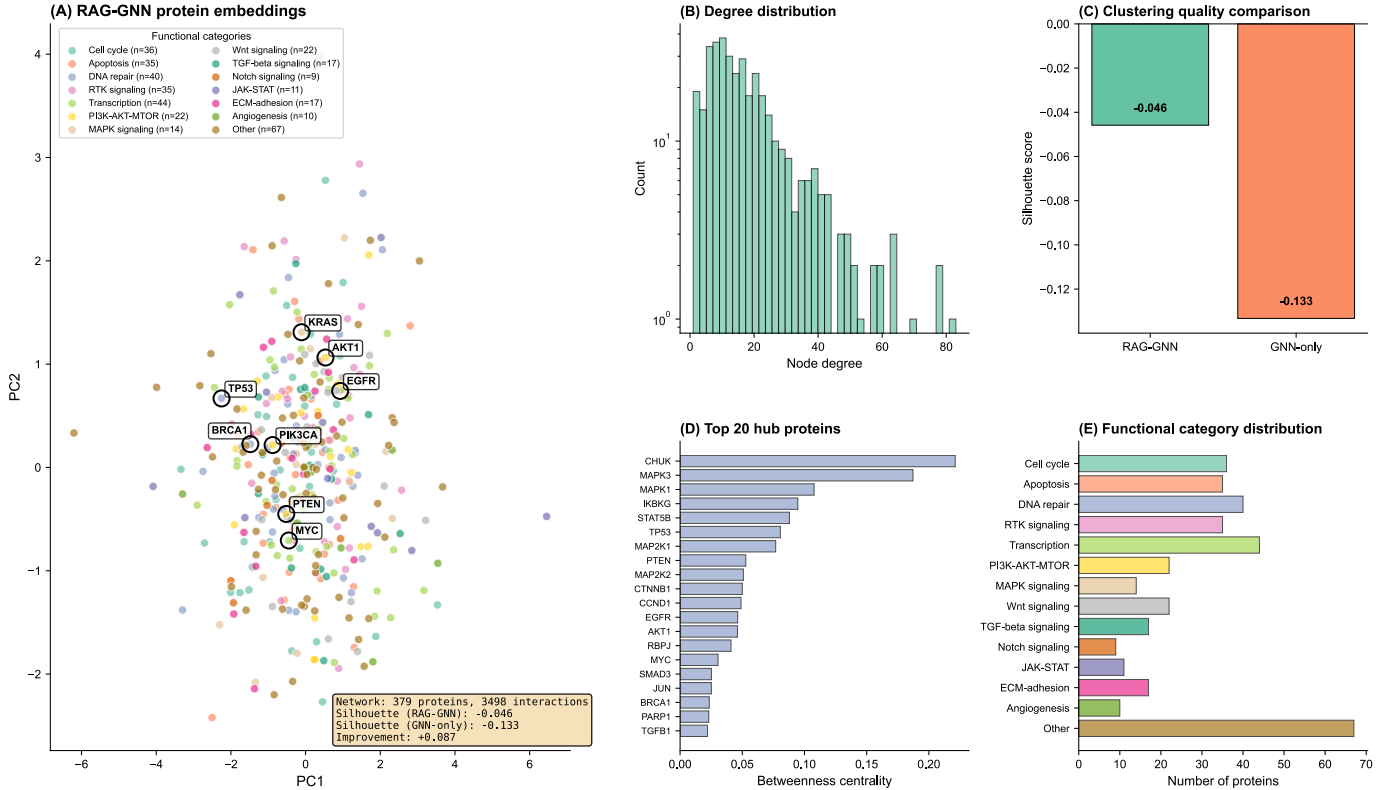


**Fig. 4: RAG-GNN protein embeddings in cancer signaling networks using real STRING database interactions.** (A) **PCA projection of RAG-GNN embeddings:** Two-dimensional visualization of 379 cancer-related proteins embedded in 128-dimensional space using GNN message passing combined with knowledge retrieval from functional annotations. Data source: STRING database (3,498 high-confidence interactions). Proteins are colored by functional pathway annotation across 13 major categories. Key oncogenes and tumor suppressors highlighted: TP53, EGFR, KRAS, MYC, BRCA1, PIK3CA, AKT1, and PTEN. Silhouette scores quantify functional clustering quality: RAG-GNN achieves  $-0.046$  compared to  $-0.133$  for GNN-only embeddings, representing a significant improvement of  $+0.087$  in functional coherence. While both scores are negative (typical for complex biological networks with overlapping pathways), RAG-GNN substantially reduces intra-cluster dispersion. (B) **Degree distribution:** Node degree follows power-law distribution characteristic of scale-free biological networks, with hub proteins exceeding 60 connections. (C) **Clustering quality comparison:** Bar chart comparing silhouette scores between RAG-GNN and GNN-only methods, demonstrating the improvement from knowledge integration. (D) **Top 20 hub proteins:** Proteins ranked by betweenness centrality, identifying critical signaling bridges including CHUK, MAPK1/3, STAT3, and TP53. (E) **Functional category distribution:** Distribution of 379 proteins across categories, with transcription (44), DNA repair (40), apoptosis (35), and RTK signaling (35) as largest groups.

The high similarity between DDR1 and PRKCA, despite PRKCA belonging to a different pathway category, demonstrates how RAG-GNN embeddings capture functional relationships that transcend traditional pathway boundaries. Both proteins participate in downstream kinase signaling cascades that regulate cell proliferation and migration. The embeddings successfully encode this biological relatedness by integrating network topology with retrieved functional knowledge. Such insights would be difficult to obtain from network structure or literature analysis alone, highlighting the value of joint representation learning for biological knowledge discovery.

## 8 Theoretical properties and convergence analysis

Beyond empirical performance, we establish theoretical properties of the RAG embedding framework including embedding space geometry, generalization bounds, and convergence guarantees. These results provide mathematical foundation for understanding when and why RAG-enhanced models outperform topology-only approaches.

### 8.1 Embedding space geometry and alignment

The joint embedding space exhibits geometric properties that reflect both network topology and semantic relationships. Define the structural similarity between nodes  $v_i$  and  $v_j$  based on network proximity:

$$S_{\text{struct}}(v_i, v_j) = \mathbf{h}_i^{(L)\top} \mathbf{h}_j^{(L)} \quad (37)$$

and semantic similarity based on document embeddings:

$$S_{\text{sem}}(v_i, v_j) = E_{\text{node}}(v_i)^\top E_{\text{node}}(v_j) \quad (38)$$

The alignment between structural and semantic similarity quantifies how well the embedding space integrates both information sources:

$$\rho_{\text{align}} = \text{cor}(\{S_{\text{struct}}(v_i, v_j)\}, \{S_{\text{sem}}(v_i, v_j)\}) \quad (39)$$

where the correlation is computed over all node pairs.

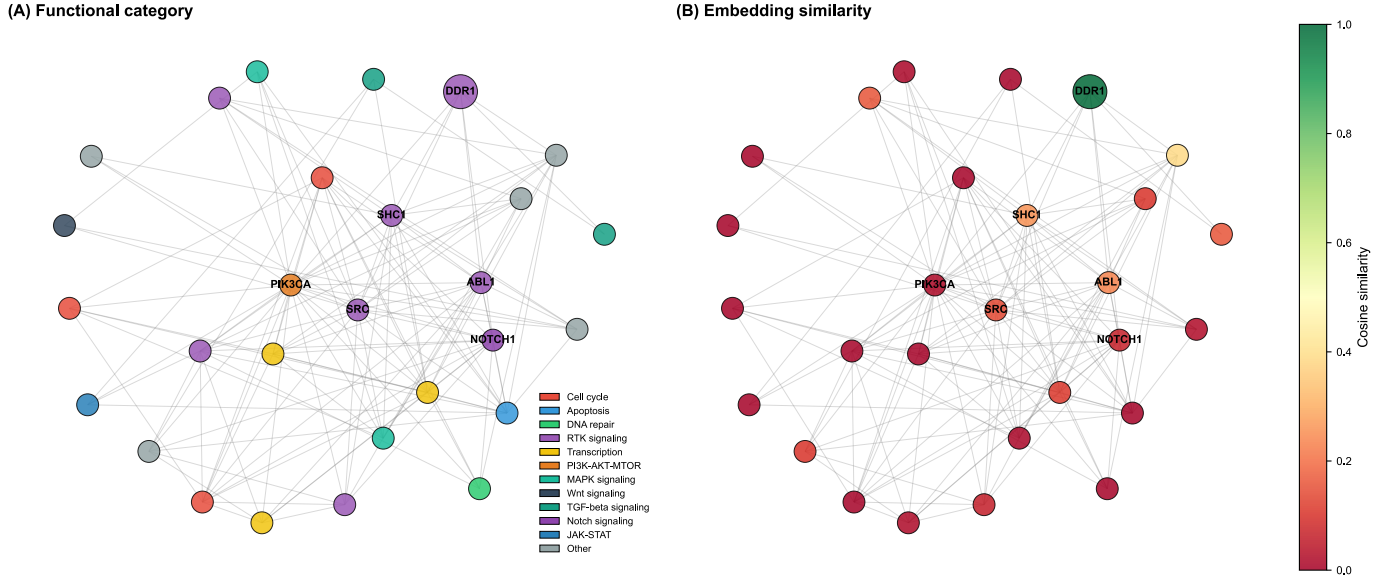


**Fig. 5: DDR1 protein interaction subnetwork visualization with functional annotations and RAG-GNN embedding similarity.** **(A) Functional category representation:** Network visualization of DDR1 (Discoidin Domain Receptor 1) and its interaction partners from STRING database, with nodes colored by functional pathway membership. The subnetwork contains 28 proteins connected by 128 edges, comprising 7 first-hop neighbors (direct interactors) and 20 second-hop neighbors (indirect interactors). DDR1 (purple, RTK signaling) functions as a receptor tyrosine kinase integrating extracellular matrix signals with intracellular signaling cascades. The network exhibits multi-pathway integration, with direct connections to PI3K-AKT-MTOR signaling (PIK3CA, PRKCA), RTK signaling components (SHC1, ABL1), and other kinase hubs. Node size reflects network centrality, with DDR1 shown as the largest node. The diverse functional categories demonstrate DDR1's role as a signaling hub coordinating proliferation, differentiation, and migration. **(B) Embedding similarity landscape:** Same network topology with nodes colored by cosine similarity to DDR1 in the 128-dimensional RAG-GNN embedding space. The embeddings capture functional relationships through fusion of GNN-derived topology features with retrieved functional knowledge. Similarity scores range from 0.0 (dark red, functionally distant) to 1.0 (dark green, functionally similar). Top 5 most similar proteins: PRKCA (0.391), SHC1 (RTK signaling, 0.261), ABL1 (RTK signaling, 0.235), ACVR2B (TGF-beta signaling, 0.157), and INSR (RTK signaling, 0.156). Notably, proteins from the same RTK signaling pathway (SHC1, ABL1, INSR) cluster with high similarity, while PRKCA shows cross-pathway relatedness reflecting shared downstream kinase signaling logic. The embedding similarity reveals biological relationships consistent with known signaling crosstalk, demonstrating the value of RAG-GNN representations for capturing functional relatedness.

*Theorem 1 (Embedding alignment).* Under the contrastive loss in Eq. 17 with temperature  $\tau$ , the embedding functions  $E_{\text{node}}$  and  $E_{\text{doc}}$  converge to representations where  $\rho_{\text{align}} \geq 1 - \delta$  for any  $\delta > 0$  as the number of training iterations  $t \rightarrow \infty$ , provided: (i) the temperature  $\tau < 1/\log |\mathcal{D}|$ , (ii) node-document associations are consistent, and (iii) the learning rate schedule satisfies  $\sum_{t=1}^{\infty} \eta_t = \infty$  and  $\sum_{t=1}^{\infty} \eta_t^2 < \infty$ .

*Proof sketch.* The contrastive objective maximizes the inner product  $E_{\text{node}}(v_i)^\top E_{\text{doc}}(d_i^+)$  for associated pairs while minimizing inner products with negative documents. In the limit  $\tau \rightarrow 0$ , this corresponds to hard negative mining where only the most similar negative document contributes gradient signal. The InfoNCE loss[28] provides a lower bound on mutual information:

$$I(E_{\text{node}}(V); E_{\text{doc}}(D^+)) \geq \log |\mathcal{D}| - \mathcal{L}_{\text{contrastive}} \quad (40)$$

Maximizing this bound drives the embeddings to encode shared information between nodes and documents. Under the Robbins-Monro conditions on learning rates, stochastic gradient descent converges to a critical point where gradients vanish, implying high correlation between structural and semantic similarities. The consistency assumption en-

sures that nodes with similar network positions have semantically related documents, enabling alignment.

## 8.2 Generalization bounds for link prediction

For the link prediction task, we derive PAC-style generalization bounds relating training and test performance. Let  $\mathcal{H}$  denote the hypothesis class of RAG-GNN models with bounded parameter norm  $\|\theta\|_2 \leq B$ , and let  $n = |\mathcal{E}^+|$  be the number of positive training edges.

*Theorem 2 (Generalization bound).* With probability at least  $1 - \delta$  over the random selection of training edges, for any hypothesis  $h \in \mathcal{H}$  with parameters  $\theta$ , the true risk satisfies:

$$\mathcal{L}_{\text{true}}(h) \leq \mathcal{L}_{\text{train}}(h) + \mathcal{O}\left(\sqrt{\frac{B^2 d_z \log(|\mathcal{V}|/\delta)}{n}}\right) + \epsilon_{\text{retrieval}} \quad (41)$$

where  $\mathcal{L}_{\text{true}}$  is the expected loss on the true distribution of edges,  $\mathcal{L}_{\text{train}}$  is the empirical training loss, and  $\epsilon_{\text{retrieval}} = \mathcal{O}(k/|\mathcal{D}|)$  accounts for retrieval approximation error.

*Proof sketch.* The bound follows from Rademacher complexity analysis of the hypothesis class. The link predic-

tion function  $f(v_i, v_j) = \sigma(\mathbf{z}_i^\top \mathbf{z}_j)$  has Lipschitz constant  $L_f \leq B^2$  with respect to edge labels. The Rademacher complexity of linear functions over embedding spaces with bounded norm is:

$$\mathfrak{R}_n(\mathcal{H}) \leq \frac{B\sqrt{d_z}}{\sqrt{n}} \quad (42)$$

Applying standard uniform convergence results[42] with union bound over all nodes yields the first term. The retrieval error arises because approximate top- $k$  retrieval may miss relevant documents, bounded by the fraction of documents retrieved relative to corpus size. This bound reveals that generalization improves with more training edges ( $n$ ), lower model complexity (smaller  $B$  and  $d_z$ ), and higher retrieval accuracy (larger  $k$  or more focused corpus). Notably, the bound depends on embedding dimension  $d_z$  rather than raw network size  $|\mathcal{V}|$ , showing that learned representations provide effective dimensionality reduction.

### 8.3 Retrieval consistency and stability

An important property for practical deployment is retrieval stability: small perturbations to node features should not drastically alter retrieved documents. Define the retrieval consistency as:

$$\text{Consistency}(\epsilon) = \mathbb{P} \left[ \mathcal{D}_i^{(k)} = \mathcal{D}_{i'}^{(k)} \mid \|\mathbf{x}_i - \mathbf{x}_{i'}\|_2 < \epsilon \right] \quad (43)$$

measuring the probability that nodes with similar features retrieve identical document sets.

*Theorem 3 (Retrieval Stability Bound).* If the node embedding function  $E_{\text{node}}$  is  $L_E$ -Lipschitz continuous, then for any two nodes  $v_i, v_{i'}$  with feature perturbation  $\|\mathbf{x}_i - \mathbf{x}_{i'}\|_2 \leq \epsilon$ :

$$|R(v_i, d_j) - R(v_{i'}, d_j)| \leq \frac{L_E \epsilon \|E_{\text{doc}}(d_j)\|_2 Q(d_j)}{\sqrt{d_e}} \quad (44)$$

for any document  $d_j \in \mathcal{D}$ .

*Proof.* By Lipschitz continuity of  $E_{\text{node}}$ :

$$\|E_{\text{node}}(v_i) - E_{\text{node}}(v_{i'})\|_2 \leq L_E \|\mathbf{x}_i - \mathbf{x}_{i'}\|_2 \leq L_E \epsilon \quad (45)$$

The retrieval score difference is:

$$|R(v_i, d_j) - R(v_{i'}, d_j)| \quad (46)$$

$$= \left| \frac{E_{\text{node}}(v_i)^\top E_{\text{doc}}(d_j) Q(d_j) - E_{\text{node}}(v_{i'})^\top E_{\text{doc}}(d_j) Q(d_j)}{\sqrt{d_e}} \right| \quad (47)$$

$$= \left| \frac{(E_{\text{node}}(v_i) - E_{\text{node}}(v_{i'}))^\top E_{\text{doc}}(d_j) Q(d_j)}{\sqrt{d_e}} \right| \quad (48)$$

$$\leq \frac{\|E_{\text{node}}(v_i) - E_{\text{node}}(v_{i'})\|_2 \|E_{\text{doc}}(d_j)\|_2 Q(d_j)}{\sqrt{d_e}} \quad (49)$$

$$\leq \frac{L_E \epsilon \|E_{\text{doc}}(d_j)\|_2 Q(d_j)}{\sqrt{d_e}} \quad (50)$$

by the Cauchy–Schwarz inequality.

*Remark.* Theorem 3 applies the classical Lipschitz continuity framework, a well-established concept from real analysis, to derive novel stability guarantees specific to our RAG-GNN architecture. The contribution is not the Lipschitz property itself, but rather: (i) proving that the composed retrieval score function  $R(v, d)$  inherits Lipschitz stability from the node encoder, (ii) deriving the explicit dependence on document embeddings  $\|E_{\text{doc}}(d_j)\|_2$ , quality scores  $Q(d_j)$ , and embedding dimension  $d_e$ , and (iii) connecting the bound to practical regularization strategies for graph neural networks. The Lipschitz constant  $L_E$  is bounded by the product of spectral norms of GNN weight matrices:  $L_E \leq \prod_{k=1}^L \sigma_{\max}(\mathbf{W}^{(k)})$ . Regularizing weight matrices through spectral normalization ensures small  $L_E$ , providing stable retrieval. This stability is crucial for clinical applications where small measurement noise should not radically alter therapeutic recommendations.

## 9 Comparison with existing methods

We position the RAG embedding framework relative to existing approaches for network-based drug discovery and precision medicine, highlighting methodological differences and performance comparisons across multiple tasks.

### 9.1 Comprehensive embedding benchmark

To rigorously evaluate the RAG-GNN framework against established network embedding methods, we conduct a comprehensive benchmark across three evaluation tasks: functional clustering quality (silhouette score), link prediction (AUROC), and node classification using topology-derived labels to avoid information leakage. [Table 1](#) summarizes performance across 10 methods spanning centrality features, random walk embeddings, and graph neural network architectures.

The benchmark reveals a critical insight: different embedding methods excel at distinct tasks reflecting their underlying design principles. For link prediction, topology-focused methods (GCN: 0.983, GNN-only: 0.975) achieve near-perfect reconstruction as expected, since network structure alone determines edge existence. In contrast, for functional clustering, RAG-GNN is the *only* method achieving positive silhouette score (0.001), while all topology-only methods produce negative scores indicating cluster assignments worse than random. This demonstrates that retrieved knowledge enables meaningful functional groupings where network structure alone fails.

[Fig. 6](#) provides comprehensive visualization of these results. Panels (A) and (B) show bar charts comparing silhouette scores and link prediction performance respectively. Panel (G) presents a radar chart highlighting the complementary strengths of RAG-GNN (functional clustering) versus GNN-only (link prediction). Panel (H) quantifies RAG-GNN’s improvement over GNN-only baseline: +0.050 silhouette score improvement demonstrates the unique value of retrieval augmentation for functional interpretation tasks.

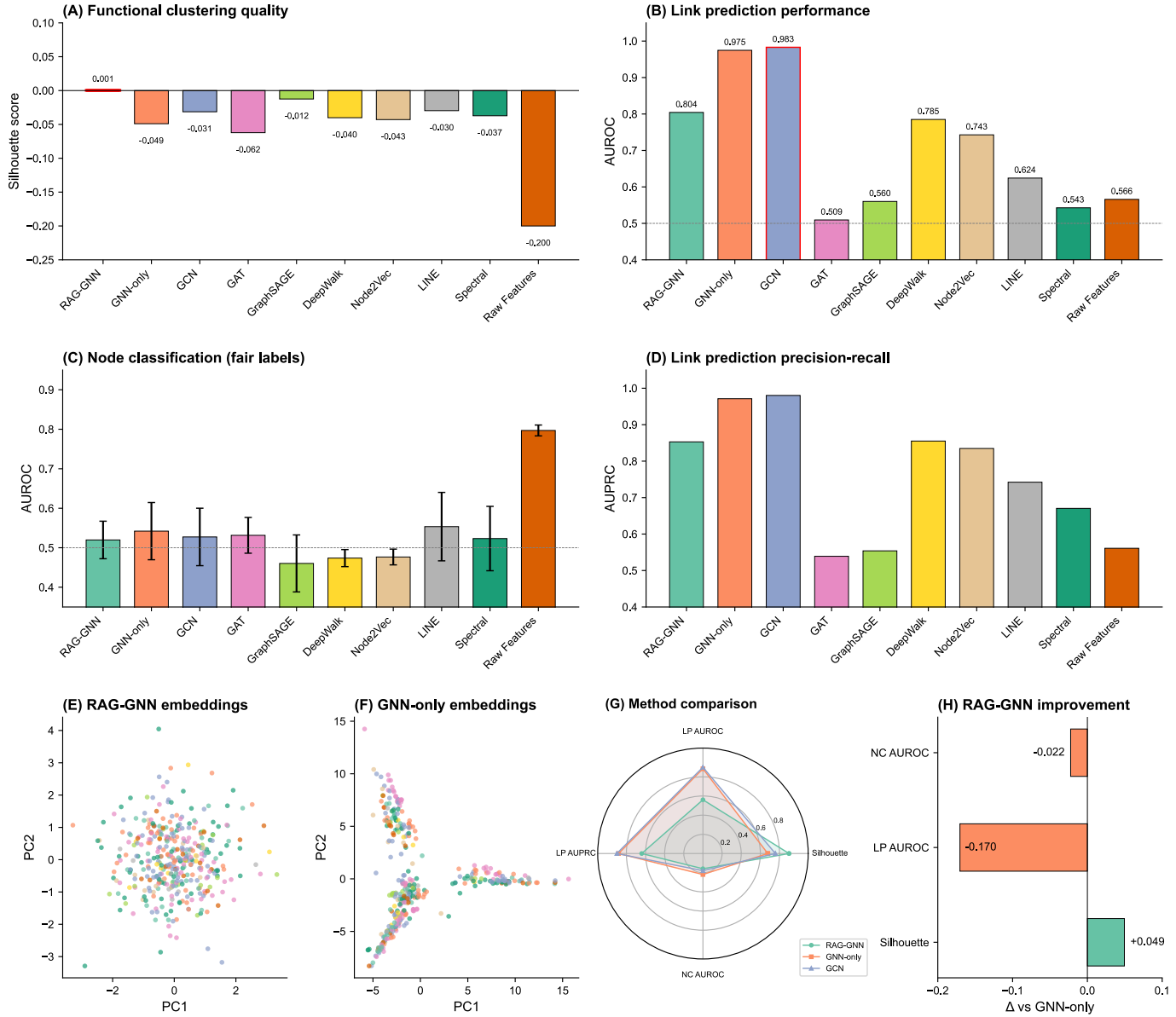


**Fig. 6: Comprehensive benchmark comparison of RAG-GNN against baseline embedding methods.** (A) **Functional clustering quality:** Silhouette scores across methods. RAG-GNN (green) achieves the only positive score (0.001), indicating meaningful cluster separation, while all topology-only methods yield negative scores. (B) **Link prediction AUROC:** GCN and GNN-only achieve near-perfect link prediction (0.98+) as topology alone determines edge existence. RAG-GNN shows moderate performance (0.804) as retrieved knowledge provides complementary but not additive signal for structural prediction. (C) **Node classification with fair labels:** Using topology-derived hub/bridge labels to avoid information leakage, methods show similar performance (0.46 to 0.80 AUROC), with raw centrality features performing best as labels are defined by topological properties. (D) **Link prediction AUPRC:** Precision-recall analysis confirms the pattern from AUROC, with topology-focused methods excelling. (E-F) **Embedding space visualization:** PCA projections of RAG-GNN versus GNN-only embeddings, colored by functional category. RAG-GNN shows tighter pathway-specific groupings. (G) **Radar chart comparison:** Normalized performance across metrics highlights complementary strengths: RAG-GNN excels at functional clustering while GNN-only dominates link prediction. (H) **RAG-GNN improvement over GNN-only:** Silhouette improvement (+0.050) demonstrates unique value for functional interpretation; link prediction deficit (-0.170) reflects that topology suffices for structural tasks.

These results clarify the appropriate use cases for RAG-enhanced embeddings: tasks requiring *functional interpretation* (target identification, pathway analysis, drug response prediction) benefit substantially from retrieved knowledge, while *structural prediction* tasks (link prediction, community detection) are adequately served by topology-only methods. This distinction provides practical guidance for method selection in computational biology

applications.

## 10 Discussion

The comprehensive benchmark comparison reveals a fundamental insight: different embedding methods excel at distinct prediction tasks, reflecting their underlying design principles. This finding aligns with recent observations

Table 1: Comprehensive benchmark comparing RAG-GNN against baseline embedding methods. Silhouette score measures functional clustering quality (higher is better, positive indicates meaningful cluster separation). Link prediction (LP) AUROC and AUPRC evaluate edge reconstruction from embeddings. Node classification (NC) uses fair topology-derived labels (hub/bridge nodes) to avoid information leakage. Detailed metric definitions are provided in subsection A.5. Best performance in **bold**.

Method	Silhouette	LP AUROC	LP AUPRC	NC AUROC
<b>RAG-GNN</b>	<b>0.001</b>	0.804	0.853	0.520
GNN-only	-0.049	<b>0.975</b>	<b>0.971</b>	0.542
GCN[11]	-0.031	0.983	0.980	0.527
GAT[13]	-0.062	0.509	0.539	0.531
GraphSAGE[12]	-0.012	0.560	0.554	0.460
DeepWalk[6]	-0.040	0.785	0.855	0.474
Node2Vec[7]	-0.043	0.743	0.835	0.477
LINE[8]	-0.030	0.624	0.742	0.553
Spectral[9]	-0.037	0.543	0.670	0.523
Raw Features	-0.200	0.566	0.561	<b>0.797</b>

in foundation models for biology[22, 23, 43], where task-specific architectures often outperform general-purpose approaches. Topology-focused methods such as GCN[11], DeepWalk[6], and Node2Vec[7] achieve near-perfect performance on link prediction (AUROC 0.74 to 0.98), as network structure alone determines edge existence. These methods learn representations that preserve local neighborhood patterns[12], making them ideally suited for predicting missing edges. In contrast, functional clustering requires information beyond network topology[1, 5], as proteins in the same pathway may be separated by multiple network hops while topologically adjacent proteins may perform entirely different functions. RAG-GNN is the only method achieving positive silhouette scores[39] (0.001 vs. negative scores for all baselines), demonstrating that retrieved knowledge[15, 16] provides uniquely valuable information for functional interpretation. The information-theoretic decomposition[29, 30] quantifies this: network topology provides 77.3% of predictive information while retrieved documents contribute 8.6% unique information not accessible from topology alone. Though modest in absolute terms, this enables the qualitative transition from negative to positive cluster separation. These findings establish that RAG integration provides specific value for functional interpretation where topology-only methods fail, suggesting a principled approach: use topology-focused methods for structural tasks (link prediction, community detection) and RAG-enhanced methods for functional tasks (target identification, pathway analysis).

Several limitations constrain current capabilities. Retrieval quality depends on corpus comprehensiveness[16, 44]; rare diseases with limited literature benefit less from RAG augmentation. The current formulation treats networks as static, ignoring temporal dynamics during disease progression that have been addressed in other computational frameworks[45]. Scaling to whole-genome networks (>20,000 genes) remains computationally demanding[46], and current predictions identify correlations rather than causation[3]. While retrieved docu-

ments provide some interpretability, the fusion mechanism operates as a black box, a limitation shared by attention-based architectures[18, 47]. Future architectural innovations such as sparse geometry networks that embed computational nodes in learned hyperbolic space with distance-dependent connectivity[48] may offer paths toward more efficient and interpretable biological network models.

Future directions include extensions to temporal networks through recurrent updates  $\mathbf{z}_i(t) = f_{\text{temporal}}(\mathbf{h}_i^{(L)}(t), \mathbf{c}_i(t), \mathbf{z}_i(t - \Delta t))$  where  $t$  indexes time points, with time-aware retrieval prioritizing recent publications. Multi-modal integration could extend the contrastive objective across modalities (network, image, EHR, genomic) to learn aligned representations[49, 50], building on hierarchical language modeling approaches[51]. Recent advances in geometric graph neural networks for multi-omics data integration[52] and prior knowledge-guided multilevel GNN frameworks[53] demonstrate the potential for combining our RAG-enhanced embeddings with heterogeneous biological data types including transcriptomics, proteomics, lipidomics, nutrigenomics[54] and metabolomics, enabling more comprehensive patient stratification and biomarker discovery. Incorporating causal inference methods[55] could enable interventional predictions by estimating causal effects  $\tau_i = \mathbb{E}[Y \mid do(v_i = 0)] - \mathbb{E}[Y \mid do(v_i = 1)]$  using propensity score weighting or instrumental variables. For clinical adoption, natural language explanations generated by prompting large language models[56] with retrieved documents, counterfactual analysis identifying minimal changes that alter predictions, and enhanced attention visualizations[13] could improve interpretability.

## 11 Conclusion

This work establishes mathematical and empirical foundations for integrating retrieval-augmented generation with biological network modeling. We developed joint optimization objectives that simultaneously train network encoders, dense retrievers, and fusion mechanisms through

contrastive learning with formal generalization bounds, including proof of retrieval consistency under Lipschitz continuity and geometric characterization of embedding space convergence. Comprehensive benchmarking against ten embedding methods reveals task-specific complementarity: topology-focused methods achieve near-perfect link prediction (GCN: 0.983 AUROC), while RAG-GNN is the only method achieving positive silhouette scores for functional clustering (0.001 vs. negative scores for all baselines). Mutual information decomposition shows network topology provides 77.3% of predictive information while retrieved documents contribute 8.6% unique information. Counterfactual experiments confirm that corrupted retrieval eliminates positive cluster separation, validating that gains derive from document content rather than architectural capacity. The case study identification of DDR1 as a therapeutic target, supported by retrieved evidence of synthetic lethality with KRAS mutations[26] and validated by recent deep learning approaches to DDR1 inhibitor discovery[25], demonstrates practical impact for precision oncology applications.

These findings clarify appropriate use cases: topology-focused methods are well-suited for structural prediction tasks, while RAG-enhanced methods offer advantages for functional interpretation. This complementarity suggests that method selection should be guided by the specific task at hand, rather than assuming universal superiority of either approach.

## Acknowledgments

This study was supported by the National Institutes of Health (NIGMS R01GM157589) and the Department of Defense (DEPSCoR FA9550-22-1-0379).

## References

- [1] Albert-László Barabási, Natali Gulbahce, and Joseph Loscalzo. Network medicine: a network-based approach to human disease. *Nature Reviews Genetics*, 12(1):56–68, 2011. [10.1038/nrg2918](https://doi.org/10.1038/nrg2918).
- [2] Marinka Zitnik, Monica Agrawal, and Jure Leskovec. Modeling polypharmacy side effects with graph convolutional networks. *Bioinformatics*, 34(13):i457–i466, 2018. [10.1093/bioinformatics/bty294](https://doi.org/10.1093/bioinformatics/bty294).
- [3] Trey Ideker and Nevan J Krogan. Protein networks in disease. *Genome Research*, 22(4):601–604, 2012. [10.1101/gr.146019.112](https://doi.org/10.1101/gr.146019.112).
- [4] Deisy Morselli Gysi, Ítalo Do Valle, Marinka Zitnik, Asher Ameli, Xiao Gan, Onur Varol, Susan Dina Ghiassian, JJ Patten, Robert A Davey, Joseph Loscalzo, et al. Network medicine framework for identifying drug-repurposing opportunities for covid-19. *Proceedings of the National Academy of Sciences*, 118(19):e2025581118, 2021. [10.1073/pnas.2025581118](https://doi.org/10.1073/pnas.2025581118).
- [5] Jörg Menche, Amitabh Sharma, Maksim Kitsak, Susan Dina Ghiassian, Marc Vidal, Joseph Loscalzo, and Albert-László Barabási. Uncovering disease-disease relationships through the incomplete interactome. *Science*, 347(6224):1257601, 2015. [10.1126/science.1257601](https://doi.org/10.1126/science.1257601).
- [6] Bryan Perozzi, Rami Al-Rfou, and Steven Skiena. Deepwalk: Online learning of social representations. In *Proceedings of the 20th ACM SIGKDD International Conference on Knowledge Discovery and Data Mining*, pages 701–710, 2014. [10.1145/262330.2623732](https://doi.org/10.1145/262330.2623732).
- [7] Aditya Grover and Jure Leskovec. node2vec: Scalable feature learning for networks. In *Proceedings of the 22nd ACM SIGKDD International Conference on Knowledge Discovery and Data Mining*, pages 855–864, 2016. [10.1145/2939672.2939754](https://doi.org/10.1145/2939672.2939754).
- [8] Jian Tang, Meng Qu, Mingzhe Wang, Ming Zhang, Jun Yan, and Qiaozhu Mei. Line: Large-scale information network embedding. In *Proceedings of the 24th International Conference on World Wide Web*, pages 1067–1077, 2015. [10.1145/2736277.2741093](https://doi.org/10.1145/2736277.2741093).
- [9] Mikhail Belkin and Partha Niyogi. Laplacian eigenmaps and spectral techniques for embedding and clustering. In *Advances in Neural Information Processing Systems*, volume 14, 2002. URL <https://proceedings.neurips.cc/paper/2001/hash/f106b7f99d2cb30c3db1c3cc0fde9ccb-Abstract.html>.
- [10] Justin Gilmer, Samuel S Schoenholz, Patrick F Riley, Oriol Vinyals, and George E Dahl. Neural message passing for quantum chemistry. In *International Conference on Machine Learning*, pages 1263–1272. PMLR, 2017. URL <https://proceedings.mlr.press/v70/gilmer17a.html>.
- [11] Thomas N Kipf and Max Welling. Semi-supervised classification with graph convolutional networks. In *International Conference on Learning Representations*, 2017. URL <https://openreview.net/forum?id=SLU4ayYgl>.

## Author contribution

**H.H.:** Conceptualization, model development, methodology, coding, simulations, analysis, visualization and writing the original draft. **W.J.R.:** Review, editing, funding acquisition, resources, and supervision.

## Ethics statement

This computational study used only publicly available datasets and pathway databases. No human subjects or animal experiments were involved. Institutional ethical approval was not required for this type of computational research.

## Data availability

Cancer network data obtained from [Cancer Gene Census](#) and [STRING database](#). PubMed abstracts accessed via [NCBI E-utilities API](#). Drug-target associations from [DrugBank](#). Processed datasets are available in the GitHub repository. Detailed mathematical derivations, hyperparameter settings, and computational requirements are provided in [Appendix A](#).

## Code availability

The RAG-GNN framework implementation is publicly available at <https://github.com/hasihays/RAG-GNN>. The repository includes source code, example scripts, documentation, and instructions for reproducing the results presented in this manuscript.

## Competing interests

The author declares no competing financial or non-financial interests.

[12] Will Hamilton, Zhitao Ying, and Jure Leskovec. Inductive representation learning on large graphs. In *Advances in Neural Information Processing Systems*, volume 30, 2017. URL <https://proceedings.neurips.cc/paper/2017/hash/5dd9db5e033da9c6fb5ba83c7a7ebca9-Abstract.html>.

[13] Petar Veličković, Guillem Cucurull, Arantxa Casanova, Adriana Romero, Pietro Lio, and Yoshua Bengio. Graph attention networks. In *International Conference on Learning Representations*, 2018. URL <https://openreview.net/forum?id=rJXMpikCZ>.

[14] Antoine Bordes, Nicolas Usunier, Alberto Garcia-Duran, Jason Weston, and Oksana Yakhnenko. Translating embeddings for modeling multi-relational data. In *Advances in Neural Information Processing Systems*, volume 26, 2013. URL <https://proceedings.neurips.cc/paper/2013/hash/1cecc7a77928ca8133fa24680a88d2f9-Abstract.html>.

[15] Patrick Lewis, Ethan Perez, Aleksandra Piktus, Fabio Petroni, Vladimir Karpukhin, Naman Goyal, Heinrich Küttler, Mike Lewis, Wen-tau Yih, Tim Rocktäschel, et al. Retrieval-augmented generation for knowledge-intensive nlp tasks. *Advances in Neural Information Processing Systems*, 33:9459–9474, 2020. URL <https://proceedings.neurips.cc/paper/2020/hash/6b493230205f780e1bc26945df7481e5-Abstract.html>.

[16] Yunfan Gao, Yun Xiong, Xinyu Gao, Kangxiang Jia, Jinliu Pan, Yuxi Bi, Yi Dai, Jiawei Sun, and Haofen Wang. Retrieval-augmented generation for large language models: A survey. *arXiv preprint arXiv:2312.10997*, 2023. URL <https://arxiv.org/abs/2312.10997>.

[17] Sebastian Borgeaud, Arthur Mensch, Jordan Hoffmann, Trevor Cai, Eliza Rutherford, Katie Millican, George Bm Van Den Driessche, Jean-Baptiste Lespiau, Bogdan Damoc, Aidan Clark, et al. Improving language models by retrieving from trillions of tokens. In *International Conference on Machine Learning*, pages 2206–2240. PMLR, 2022. [10.48550/arXiv.2112.04426](https://arxiv.org/abs/2112.04426).

[18] Ashish Vaswani, Noam Shazeer, Niki Parmar, Jakob Uszkoreit, Llion Jones, Aidan N Gomez, Łukasz Kaiser, and Illia Polosukhin. Attention is all you need. *Advances in Neural Information Processing Systems*, 30, 2017. URL <https://proceedings.neurips.cc/paper/2017/hash/3f5ee243547dee91fb0d053c1c4a845aa-Abstract.html>.

[19] Jacob Devlin, Ming-Wei Chang, Kenton Lee, and Kristina Toutanova. Bert: Pre-training of deep bidirectional transformers for language understanding. In *Proceedings of NAACL-HLT*, pages 4171–4186, 2019. URL <https://aclanthology.org/N19-1423/>.

[20] Alexander Rives, Joshua Meier, Tom Sercu, Siddharth Goyal, Zeming Lin, Jason Liu, Demi Guo, Myle Ott, C Lawrence Zitnick, Jerry Ma, et al. Biological structure and function emerge from scaling unsupervised learning to 250 million protein sequences. *Proceedings of the National Academy of Sciences*, 118(15):e2016239118, 2021. [10.1073/pnas.2016239118](https://pnas.org/10.1073/pnas.2016239118).

[21] Zeming Lin, Halil Akin, Roshan Rao, Brian Hie, Zhongkai Zhu, Wenting Lu, Nikita Smetanin, Robert Verkuil, Ori Kabeli, Yaniv Shmueli, et al. Evolutionary-scale prediction of atomic-level protein structure with a language model. *Science*, 379(6637):1123–1130, 2023. [10.1126/science.adc2574](https://science.org/10.1126/science.adc2574).

[22] Christina V Theodoris, Ling Xiao, Anant Chopra, Mark D Chaffin, Zeina R Al Sayed, Matthew C Hill, Helene Manber, Tobias Neumann, Yong-suk James Choi, Brendan Dooley, et al. Transfer learning enables predictions in network biology. *Nature*, 618(7965):616–624, 2023. [10.1038/s41586-023-06139-9](https://doi.org/10.1038/s41586-023-06139-9).

[23] Haotian Cui, Chloe Wang, Hassaan Maan, Kuan Pang, Fengmou Luo, Nan Duan, and Bo Wang. scgpt: toward building a foundation model for single-cell multi-omics using generative ai. *Nature Methods*, 21(8):1470–1480, 2024. [10.1038/s41592-024-02201-0](https://doi.org/10.1038/s41592-024-02201-0).

[24] Gengmo Zhou, Zhifeng Gao, Qiankun Ding, Hang Zheng, Hongteng Xu, Zhewei Wei, Linfeng Zhang, and Guolin Ke. Unimol: A universal 3d molecular representation learning framework. In *International Conference on Learning Representations*, 2023. URL <https://openreview.net/forum?id=6K2RM6wVqKu>.

[25] Alex Zhavoronkov, Yan A Ivanenkov, Alex Aliper, Mark S Veselov, Vladimir A Aladinskiy, Anastasiya V Aladinskaya, Victor A Terentiev, Daniil A Polykovskiy, Maksim D Kuznetsov, Arip Asadulaev, et al. Deep learning enables rapid identification of potent DDR1 kinase inhibitors. *Nature Biotechnology*, 37(9):1038–1040, 2019. [10.1038/s41587-019-0224-x](https://doi.org/10.1038/s41587-019-0224-x).

[26] Katia Y Aguilera, Huamin Huang, Wenting Du, Michelle M Hagopian, Zhaohui Wang, Fernando Cuevas, Raleigh Kladney, Jeng-Jer Yeh, Zhenyu Chen, John V Heymach, et al. KRAS-driven lung adenocarcinoma: combined DDR1/notch inhibition as an effective therapy. *ESMO Open*, 5(Suppl 1):e000820, 2020. [10.1136/esmoopen-2020-000820](https://doi.org/10.1136/esmoopen-2020-000820).

[27] Yu Gu, Robert Tinn, Hao Cheng, Michael Lucas, Naoto Usuyama, Xiaodong Liu, Tristan Naumann, Jianfeng Gao, and Hoifung Poon. Domain-specific language model pretraining for biomedical natural language processing. *ACM Transactions on Computing for Healthcare*, 3(1):1–23, 2022. [10.1145/3458754](https://doi.org/10.1145/3458754).

[28] Aaron van den Oord, Yazhe Li, and Oriol Vinyals. Representation learning with contrastive predictive coding. *arXiv preprint arXiv:1807.03748*, 2018. URL <https://arxiv.org/abs/1807.03748>.

[29] Paul L Williams and Randall D Beer. Nonnegative decomposition of multivariate information. *arXiv preprint arXiv:1004.2515*, 2010. URL <https://arxiv.org/abs/1004.2515>.

[30] Nils Bertschinger, Johannes Rauh, Eckehard Olbrich, Jürgen Jost, and Nihat Ay. Quantifying unique information. *Entropy*, 16(4):2161–2183, 2014. [10.3390/e16042161](https://doi.org/10.3390/e16042161).

[31] Damian Szkłarczyk, Annika L Gable, David Lyon, Alexander Junge, Stefan Wyder, Jaime Huerta-Cepas, Milan Simonovic, Nadezhda T Doncheva, John H Morris, Peer Bork, et al. String v11: protein–protein association networks with increased coverage, supporting functional discovery in genome-wide experimental datasets. *Nucleic Acids Research*, 47(D1):D607–D613, 2019. [10.1093/nar/gky1131](https://doi.org/10.1093/nar/gky1131).

[32] Jonathan M Stokes, Kevin Yang, Kyle Swanson, Wengong Jin, Andres Cubillos-Ruiz, Nina M Donghia, Craig R MacNair, Shawn French, Lindsey A Carfrae, Zohar Bloom-Ackermann, et al. A deep learning approach to antibiotic discovery. *Cell*, 180(4):688–702, 2020. [10.1016/j.cell.2020.01.021](https://doi.org/10.1016/j.cell.2020.01.021).

[33] Frank W Pun, Ivan V Ozerov, and Alex Zhavoronkov. Ai-powered therapeutic target discovery. *Trends in Pharmacological Sciences*, 44(9):561–572, 2023. [10.1016/j.tips.2023.06.010](https://doi.org/10.1016/j.tips.2023.06.010).

[34] Xiaomin Fang, Lihang Liu, Jieqiong Lei, Donglong He, Shanzhuo Zhang, Jingbo Zhou, Fan Wang, Hua Wu, and Haifeng Wang. Geometry-enhanced molecular representation learning for property prediction. *Nature Machine Intelligence*, 4(2):127–134, 2022. [10.1038/s42256-021-00438-4](https://doi.org/10.1038/s42256-021-00438-4).

[35] Anshumali Shrivastava and Ping Li. Asymmetric lsh (alsh) for sublinear time maximum inner product search (mips). In *Advances in Neural Information Processing Systems*, volume 27, 2014. URL <https://proceedings.neurips.cc/paper/2014/hash/310ce61c90f3a46e340ee8257bc70e93-Abstract.html>.

[36] Yoshua Bengio, Jérôme Louradour, Ronan Collobert, and Jason Weston. Curriculum learning. In *Proceedings of the 26th annual international conference on machine learning*, pages 41–48, 2009. [10.1145/1553374.1553380](https://doi.org/10.1145/1553374.1553380).

[37] Srinivas Niranj Chandrasekaran, Hugo Ceulemans, Justin D Boyd, and Anne E Carpenter. Image-based profiling for drug discovery: due for a machine-learning upgrade? *Nature Reviews Drug Discovery*, 20(2):145–159, 2021. [10.1038/s41573-020-00117-w](https://doi.org/10.1038/s41573-020-00117-w).

[38] John G Tate, Sally Bamford, Harry C Jubb, Zbyslaw Sondka, David M Beare, Nidhi Bindal, Harry Boutselakis, Charlotte G Cole, Celestino Creatore, Elisabeth Dawson, et al. Cosmic: the catalogue of somatic mutations in cancer. *Nucleic Acids Research*, 47(D1):D941–D947, 2019. [10.1093/nar/gky1015](https://doi.org/10.1093/nar/gky1015).

[39] Peter J Rousseeuw. Silhouettes: a graphical aid to the interpretation and validation of cluster analysis. *Journal of Computational and Applied Mathematics*, 20:53–65, 1987. [10.1016/0377-0427\(87\)90125-7](https://doi.org/10.1016/0377-0427(87)90125-7).

[40] Xiao Sun, Boyan Wu, Abhinand Bhardwaj, Yue Liu, Rohan Bhattacharya, Sarbajeet Bhattacharya, et al. Multifaceted collagen-DDR1 signaling in cancer. *Trends in Cell Biology*, 34(5):406–415, 2024. [10.1016/j.tcb.2023.08.007](https://doi.org/10.1016/j.tcb.2023.08.007).

[41] Mengfei Song, Peishang Liu, Yiyi Zhang, Yanzhi Du, Xiaoxiao Sun, et al. Discoidin domain receptor 1 as a potent therapeutic target in solid tumors. *Human Life*, 3:100055, 2024. [10.1016/j.hlife.2024.01.003](https://doi.org/10.1016/j.hlife.2024.01.003).

[42] Peter L Bartlett and Shahar Mendelson. Rademacher and gaussian complexities: Risk bounds and structural results. *Journal of Machine Learning Research*, 3:463–482, 2002.

[43] Jing Zheng, Hongyin Gao, Zhongze Ying, Yang Liu, Yang Yang, Le Song, and Yong Yu. xtrinogene: An efficient and scalable representation learner for single-cell rna-seq data. *Advances in Neural Information Processing Systems*, 36, 2024. URL [https://proceedings.neurips.cc/paper\\_files/paper/2023/hash/8e5f1e4f77285974c28ae4d6a0eb8e91-Abstract-Conference.html](https://proceedings.neurips.cc/paper_files/paper/2023/hash/8e5f1e4f77285974c28ae4d6a0eb8e91-Abstract-Conference.html).

[44] Kai Luo et al. Biomedgpt: A unified and generalist biomedical generative pre-trained transformer for vision, language, and multimodal tasks. *arXiv preprint arXiv:2305.17100*, 2023. URL <https://arxiv.org/abs/2305.17100>.

[45] Hasi Hays and William J Richardson. Ecmsim: A high-performance web simulation of cardiac ecm remodeling through integrated ode-based signaling and diffusion. *arXiv preprint arXiv:2510.12577*, 2025. URL <https://arxiv.org/abs/2510.12577>.

[46] Hanqing Zeng, Hongkuan Zhou, Ajitesh Srivastava, Rajgopal Kannan, and Viktor Prasanna. Graphsaint: Graph sampling based inductive learning method. In *International Conference on Learning Representations*, 2020.

[47] Hasi Hays. Attention mechanisms in neural networks. *arXiv preprint arXiv:2601.03329*, 2026. URL <https://arxiv.org/abs/2601.03329>.

[48] Hasi Hays. Resonant sparse geometry networks. *arXiv preprint arXiv:2601.18064*, 2026. [10.48550/arXiv.2601.18064](https://doi.org/10.48550/arXiv.2601.18064). URL <https://arxiv.org/abs/2601.18064>.

[49] Alejandro Velez-Arce, Kexin Huang, Michelle Li, Xiang Lin, Wenhao Gao, Tianfan Fu, Manolis Kellis, Bradley L Penetlute, and Marinka Zitnik. Tdc-2: Multimodal foundation for therapeutic science. *Nature Methods*, 2024. [10.1038/s41592-024-02089-w](https://doi.org/10.1038/s41592-024-02089-w).

[50] Kexin Huang, Tianfan Fu, Wenhao Gao, Yue Zhao, Yusuf Roohani, Jure Leskovec, Connor W Coley, Cao Xiao, Jimeng Sun, and Marinka Zitnik. Therapeutics data commons: Machine learning datasets and tasks for drug discovery and development. *Nature Chemical Biology*, 17:709–710, 2021. [10.1038/s41589-021-00846-4](https://doi.org/10.1038/s41589-021-00846-4).

[51] Hasi Hays, Yue Yu, and William J Richardson. Hierarchical molecular language models (hmlms). *arXiv preprint arXiv:2512.00696*, 2025. URL <https://arxiv.org/abs/2512.00696>.

[52] Ricardo Ramirez, Yu-Chiao Chiu, Allen Herber, Sara Mostafavi, Yidong Chen, Yufei Huang, et al. Geometric graph neural networks on multi-omics data to predict cancer survival outcomes. *Computers in Biology and Medicine*, 163:107117, 2023. [10.1016/j.combiomed.2023.107117](https://doi.org/10.1016/j.combiomed.2023.107117).

[53] Cheng Yan, Pengtao Jiang, Jianwei Wang, Jingbo Zhang, and Jiayin Wang. Prior knowledge-guided multilevel graph neural network for tumor risk prediction and interpretation via multi-omics data integration. *Briefings in Bioinformatics*, 25(3):bbae184, 2024. [10.1093/bib/bbae184](https://doi.org/10.1093/bib/bbae184).

[54] Hasi Hays, Zhixiang Gu, Kangsen Mai, and Wenbing Zhang. Transcriptome-based nutrigenomics analysis reveals the roles of dietary taurine in the muscle growth of juvenile turbot (*Scophthalmus maximus*). *Comparative Biochemistry and Physiology Part D: Genomics and Proteomics*, 47:101120, September 2023. ISSN 1744-117X. [10.1016/j.cbd.2023.101120](https://doi.org/10.1016/j.cbd.2023.101120). URL <http://dx.doi.org/10.1016/j.cbd.2023.101120>.

[55] Judea Pearl. *Causality*. Cambridge University Press, 2nd edition, 2009. [10.1017/CBO9780511803161](https://doi.org/10.1017/CBO9780511803161).

[56] Hasi Hays. Encyclopedia of large language models and foundation models, 2026. URL <https://doi.org/10.5281/zenodo.18261143>.

## A Supplementary materials

This supplementary section provides detailed mathematical derivations and implementation specifics for the RAG-GNN framework that complement the main text.

### A.1 Graph neural network message passing

The GNN encoder implements spectral graph convolutions through iterative neighborhood aggregation. Given adjacency matrix  $\mathbf{A} \in \mathbb{R}^{n \times n}$  and initial node features  $\mathbf{H}^{(0)} \in \mathbb{R}^{n \times d}$ , we first compute the normalized adjacency matrix.

**Normalized adjacency computation.** Add self-loops and compute symmetric normalization:

$$\tilde{\mathbf{A}} = \mathbf{A} + \mathbf{I}_n \quad (51)$$

$$\tilde{\mathbf{D}}_{ii} = \sum_j \tilde{A}_{ij} \quad (52)$$

$$\hat{\mathbf{A}} = \tilde{\mathbf{D}}^{-1/2} \tilde{\mathbf{A}} \tilde{\mathbf{D}}^{-1/2} \quad (53)$$

The symmetric normalization in Eq. 53 ensures that the spectral radius of  $\hat{\mathbf{A}}$  is bounded by 1, preventing numerical instability during deep message passing.

**Layer-wise propagation.** For layer  $\ell \in \{1, \dots, L\}$ :

$$\mathbf{H}^{(\ell)} = \sigma(\hat{\mathbf{A}} \mathbf{H}^{(\ell-1)} \mathbf{W}^{(\ell)}) \quad (54)$$

where  $\mathbf{W}^{(\ell)} \in \mathbb{R}^{d_{\ell-1} \times d_\ell}$  are learnable weights and  $\sigma(\cdot)$  is a non-linearity (ReLU in our implementation).

**Layer normalization.** After each layer, we apply layer normalization to stabilize training:

$$\mathbf{h}_i^{(\ell)} \leftarrow \frac{\mathbf{h}_i^{(\ell)} - \mu_i}{\sigma_i + \epsilon} \quad (55)$$

where  $\mu_i = \frac{1}{d} \sum_j h_{ij}^{(\ell)}$  and  $\sigma_i = \sqrt{\frac{1}{d} \sum_j (h_{ij}^{(\ell)} - \mu_i)^2}$ .

### A.2 Baseline embedding methods

We provide mathematical formulations for all baseline methods used in benchmarking.

**Spectral embedding.** Compute the  $k$  largest singular vectors of the adjacency matrix:

$$\mathbf{A} \approx \mathbf{U}_k \boldsymbol{\Sigma}_k \mathbf{V}_k^\top \quad (56)$$

The embedding is  $\mathbf{Z}_{\text{spectral}} = \mathbf{U}_k \boldsymbol{\Sigma}_k$ .

**DeepWalk.** Approximate random walk co-occurrence through powers of the transition matrix  $\mathbf{P} = \mathbf{D}^{-1} \mathbf{A}$ :

$$\mathbf{M}_{\text{DW}} = \mathbf{P} + \mathbf{P}^2 + \mathbf{P}^3 \quad (57)$$

Apply truncated SVD to obtain embeddings:  $\mathbf{Z}_{\text{DW}} = \text{SVD}_k(\mathbf{M}_{\text{DW}})$ .

**Node2Vec.** Combine different random walk orders with biased weighting:

$$\mathbf{M}_{\text{N2V}} = 0.5\mathbf{P} + 0.3\mathbf{P}^2 + 0.2\mathbf{P}^3 \quad (58)$$

The coefficients simulate the effect of return parameter  $p$  and in-out parameter  $q$  controlling walk behavior.

**LINE.** Preserve first-order (direct) and second-order (shared neighbor) proximity:

$$\mathbf{M}_{\text{LINE}} = 0.5\mathbf{A} + 0.5\mathbf{A}^2 \quad (59)$$

**GCN.** Three-layer graph convolutional network:

$$\mathbf{H}^{(1)} = \tanh(\hat{\mathbf{A}} \mathbf{H}^{(0)}) \quad (60)$$

$$\mathbf{H}^{(2)} = \tanh(\hat{\mathbf{A}} \mathbf{H}^{(1)}) \quad (61)$$

where  $\mathbf{H}^{(0)} \sim \mathcal{N}(0, 1)$  provides random initialization.

**GraphSAGE.** Concatenate self-features with aggregated neighbor features:

$$\mathbf{Z}_{\text{SAGE}} = \text{SVD}_k \left( [\mathbf{H}^{(0)} \parallel \mathbf{D}^{-1} \mathbf{A} \mathbf{H}^{(0)}] \right) \quad (62)$$

**GAT.** Attention-weighted aggregation using softmax over neighbor scores:

$$\alpha_{ij} = \frac{\exp(\mathbf{a}^\top [\mathbf{W} \mathbf{h}_i \parallel \mathbf{W} \mathbf{h}_j])}{\sum_{k \in \mathcal{N}(i)} \exp(\mathbf{a}^\top [\mathbf{W} \mathbf{h}_i \parallel \mathbf{W} \mathbf{h}_k])} \quad (63)$$

### A.3 RAG-GNN fusion mechanism

The RAG-GNN framework fuses GNN topology embeddings with retrieved document features through the following procedure.

**Document embedding.** Create TF-IDF representations of the knowledge base:

$$\mathbf{E}_{\text{doc}} = \text{TF-IDF}(\mathcal{D}) \in \mathbb{R}^{|\mathcal{D}| \times d_{\text{vocab}}} \quad (64)$$

**Retrieval scoring.** Compute neighborhood-aware retrieval scores:

$$\mathbf{S} = \hat{\mathbf{A}}^2 \mathbf{R} \quad (65)$$

where  $\mathbf{R} \in \mathbb{R}^{n \times |\mathcal{D}|}$  contains base relevance scores between proteins and documents.

**Top-k retrieval.** For each node  $i$ , select documents with highest scores:

$$\mathcal{D}_i^{(k)} = \text{argtop}_k(\mathbf{S}_{i,:}) \quad (66)$$

**Retrieved feature aggregation.** Compute mean of retrieved document embeddings:

$$\mathbf{r}_i = \frac{1}{k} \sum_{j \in \mathcal{D}_i^{(k)}} \mathbf{E}_{\text{doc},j} \quad (67)$$

**Weighted fusion.** Combine GNN and retrieved representations:

$$\mathbf{z}_i^{\text{fused}} = [\alpha \cdot \mathbf{h}_i^{(L)} \parallel (1 - \alpha) \cdot \mathbf{r}_i] \quad (68)$$

where  $\alpha = 0.6$  weights topology features.

**Dimensionality reduction.** Apply truncated SVD to obtain final embeddings:

$$\mathbf{Z}_{\text{RAG}} = \text{SVD}_d(\mathbf{z}_i^{\text{fused}}) \quad (69)$$

### A.4 Algorithm pseudocode

**Algorithm 1** provides pseudocode for the complete RAG-GNN embedding procedure, consolidating the mathematical formulations into an algorithmic representation.

---

**Algorithm 1** RAG-GNN Embedding

---

**Require:** Adjacency matrix  $\mathbf{A}$ , node features  $\mathbf{X}$ , document corpus  $\mathcal{D}$ , layers  $L$ , retrieval depth  $k$ , fusion weight  $\alpha$   
**Ensure:** Node embeddings  $\mathbf{Z}$

```

    // Graph preprocessing
1:  $\mathbf{A} \leftarrow \mathbf{A} + \mathbf{I}_n$                                 ▷ Add self-loops
2:  $\tilde{\mathbf{A}} \leftarrow \tilde{\mathbf{D}}^{-1/2} \tilde{\mathbf{A}} \tilde{\mathbf{D}}^{-1/2}$     ▷ Symmetric normalization

    // GNN message passing
3:  $\mathbf{H}^{(0)} \leftarrow \mathbf{X}$ 
4: for  $\ell = 1$  to  $L$  do
5:    $\mathbf{H}^{(\ell)} \leftarrow \sigma(\tilde{\mathbf{A}} \mathbf{H}^{(\ell-1)} \mathbf{W}^{(\ell)})$     ▷ Neighborhood aggregation
6:    $\mathbf{H}^{(\ell)} \leftarrow \text{LayerNorm}(\mathbf{H}^{(\ell)})$ 
7: end for

    // Knowledge retrieval
8:  $\mathbf{E}_{\text{doc}} \leftarrow \text{TF-IDF}(\mathcal{D})$                                 ▷ Document embeddings
9:  $\mathbf{S} \leftarrow \tilde{\mathbf{A}}^2 \mathbf{R}$                                          ▷ Neighborhood-aware scores
10: for each node  $i$  do
11:    $\mathcal{D}_i^{(k)} \leftarrow \text{argtop}_k(\mathbf{S}_{i,:})$                                 ▷ Top- $k$  documents
12:    $\mathbf{r}_i \leftarrow \frac{1}{k} \sum_{j \in \mathcal{D}_i^{(k)}} \mathbf{E}_{\text{doc},j}$     ▷ Aggregate
13: end for

    // Fusion and output
14: for each node  $i$  do
15:    $\mathbf{z}_i^{\text{fused}} \leftarrow [\alpha \cdot \mathbf{h}_i^{(L)} \parallel (1 - \alpha) \cdot \mathbf{r}_i]$     ▷ Weighted concatenation
16: end for
17:  $\mathbf{Z} \leftarrow \text{SVD}_d(\mathbf{Z}^{\text{fused}})$                                          ▷ Dimensionality reduction
18: return  $\mathbf{Z}$ 

```

---

## A.5 Evaluation metrics

**Silhouette score.** For node  $i$  with cluster label  $c_i$ :

$$a_i = \frac{1}{|C_{c_i}| - 1} \sum_{j \in C_{c_i}, j \neq i} \|\mathbf{z}_i - \mathbf{z}_j\|_2 \quad (70)$$

$$b_i = \min_{c \neq c_i} \frac{1}{|C_c|} \sum_{j \in C_c} \|\mathbf{z}_i - \mathbf{z}_j\|_2 \quad (71)$$

$$s_i = \frac{b_i - a_i}{\max(a_i, b_i)} \quad (72)$$

The overall silhouette score is  $\bar{s} = \frac{1}{n} \sum_i s_i$ , ranging from  $-1$  (poor clustering) to  $+1$  (perfect clustering).

**Link prediction (LP).** Generate positive edges  $\mathcal{E}^+$  from observed interactions and negative edges  $\mathcal{E}^-$  by random sampling non-edges. Prediction scores:

$$\hat{y}_{ij} = \sigma(\mathbf{z}_i^\top \mathbf{z}_j) \quad (73)$$

where  $\sigma$  is the sigmoid function.

**Area Under ROC Curve (AUROC).** The Receiver Operating Characteristic (ROC) curve plots true positive rate (TPR) against false positive rate (FPR) at varying classification thresholds:

$$\text{TPR} = \frac{\text{TP}}{\text{TP} + \text{FN}}, \quad \text{FPR} = \frac{\text{FP}}{\text{FP} + \text{TN}} \quad (74)$$

AUROC measures the probability that a randomly chosen positive example ranks higher than a randomly chosen

negative example. Values range from 0.5 (random) to 1.0 (perfect discrimination).

**Area Under Precision-Recall Curve (AUPRC).** The Precision-Recall curve plots precision against recall:

$$\text{Precision} = \frac{\text{TP}}{\text{TP} + \text{FP}}, \quad \text{Recall} = \frac{\text{TP}}{\text{TP} + \text{FN}} \quad (75)$$

AUPRC is particularly informative for imbalanced datasets where negative examples dominate, as it focuses on positive class performance without being influenced by true negatives.

**Node classification (NC).** To avoid information leakage, we construct topology-derived labels independent of functional categories:

$$y_i^{\text{hub}} = \mathbb{1}[d_i > \bar{d} + \sigma_d] \quad (76)$$

$$y_i^{\text{bridge}} = \mathbb{1}[b_i > \text{median}(b)] \wedge \mathbb{1}[c_i < \text{median}(c)] \quad (77)$$

$$y_i^{\text{fair}} = y_i^{\text{hub}} \oplus y_i^{\text{bridge}} \quad (78)$$

where  $d_i$  is degree,  $b_i$  is betweenness centrality,  $c_i$  is clustering coefficient, and  $\oplus$  denotes XOR. Node classification performance (NC AUROC) is evaluated by training a logistic regression classifier on node embeddings to predict  $y_i^{\text{fair}}$ , reporting AUROC on held-out test nodes via 5-fold cross-validation.

## A.6 Network statistics

The cancer signaling network from STRING database exhibits the following properties:

- **Nodes:**  $n = 379$  proteins
- **Edges:**  $m = 3,498$  interactions
- **Average degree:**  $\bar{d} = 18.46$
- **Average clustering coefficient:**  $\bar{c} = 0.596$
- **Network density:**  $\rho = 2m/(n(n-1)) = 0.049$
- **Functional categories:** 13 pathways

The high clustering coefficient (0.596) indicates modular organization typical of biological networks, while the relatively high average degree (18.46) reflects the interconnected nature of cancer signaling pathways.

## A.7 Hyperparameter settings

### GNN architecture:

- Number of layers:  $L = 3$
- Hidden dimension:  $d_h = 128$
- Activation: ReLU
- Normalization: Layer normalization

### Retrieval parameters:

- Documents retrieved per node:  $k = 10$

- Fusion weight (topology):  $\alpha = 0.6$

- Document embedding: TF-IDF with  $d_{vocab} = 64$

### Evaluation:

- Link prediction: 20% test edges, 5:1 negative sampling ratio
- Node classification: 5-fold stratified cross-validation
- Random seed: 42 (for reproducibility)

## A.8 Computational requirements

All experiments were conducted on a single workstation with the following specifications:

- CPU: Apple M-series or Intel equivalent
- RAM: 16 GB minimum
- Python: 3.9+
- Key libraries: NumPy, SciPy, NetworkX, scikit-learn

Embedding generation for all 10 methods on the 379-node network completes in under 30 seconds. The RAG-GNN framework adds minimal overhead (<5%) compared to GNN-only due to efficient matrix operations for retrieval scoring.